Atmos. Chem. Phys. Discuss., 13, 28453–28510, 2013
www.atmos-chem-phys-discuss.net/13/28453/2013/
doi:10.5194/acpd-13-28453-2013

Atmospheric Chemistry and Physics Discussions

Fire emission rates of NO_x based on the empirical relationship between satellite-derived tropospheric NO_2 and fire radiative power

S. F. Schreier[1], A. Richter[1], J. W. Kaiser[2,3,4], and J. P. Burrows[1]

[1]Institute of Environmental Physics, University of Bremen, Bremen, Germany
[2]King's College London, London, UK
[3]European Centre for Medium-range Weather Forecasts, Reading, UK
[4]Max Planck Institute for Chemistry, Mainz, Germany

Received: 25 September 2013 – Accepted: 18 October 2013 – Published: 1 November 2013

Correspondence to: S. F. Schreier (schreier@iup.physik.uni-bremen.de)

Published by Copernicus Publications on behalf of the European Geosciences Union.

Abstract

Nitrogen oxides (NO_x) play key roles in atmospheric chemistry, air pollution, and climate. While the largest fraction of these reactive gases is released by anthropogenic emission sources, a significant amount can be attributed to vegetation fires. In this study, NO_2 from GOME-2 on board EUMETSAT's MetOp-A and OMI on board NASA's Aura as well as fire radiative power (FRP) from the measurements of MODIS on board NASA's Terra and Aqua are used to derive fire emission rates (FERs) of NO_x for different types of vegetation using a simple statistical approach. Monthly means of tropospheric NO_2 vertical columns (TVC NO_2) have been analyzed for their temporal correlation with the monthly means of FRP for five consecutive years from 2007 to 2011 on a horizontal $1^\circ \times 1^\circ$ grid. The strongest correlation is found to be largely confined to tropical and subtropical regions, which account for more than 80 % of yearly burned area on average globally. In these regions, the seasonal variation of fire intensity, expressed by the FRP data, is similar to the pattern of TVC NO_2. As chemical models typically require values for the amount of NO_x being released as a function of time, we have converted the retrieved TVC NO_2 into production rates of NO_x from fire (P_f) by assuming a constant lifetime of NO_x. The comparison between P_f and NO_x emissions from GFEDv3.1 over 5 characteristic biomass burning regions in the tropics and subtropics indicated good agreement. By separating the monthly means of P_f and FRP according to land cover type, FERs of NO_x could be derived for different biomes. The estimated FERs for the dominating types of vegetation burned are lowest for open shrublands and savannas (0.28–1.03 g $NO_x\,s^{-1}\,MW^{-1}$) and highest for croplands and woody savannas (0.82–1.56 g $NO_x\,s^{-1}\,MW^{-1}$). This analysis demonstrates clearly that there are biome-specific, diurnal, and regional differences in FERs for the dominating types of vegetation burned in the tropics and subtropics. Possible factors affecting the magnitude of the obtained values are discussed.

ACPD
13, 28453–28510, 2013

1 Introduction

Nitrogen oxides (NO_x = NO+NO_2) enter the atmosphere from a large number of natural and anthropogenic processes. Nitric oxide (NO) and nitrogen dioxide (NO_2) are coupled in the atmosphere as NO_2 is photolyzed to produce NO and an oxygen atom (O), which then reacts with molecular oxygen (O_2) to produce ozone (O_3). Major sources of NO_x are attributed to anthropogenic activities (e.g. high temperature combustion processes), biomass burning (intentional and accidental), soil microbial production from the oxidation of ammonium ions (NH_4^+) and the reduction of nitrate ions (NO_3^-), and lightning strikes (Lee et al., 1997). Minor tropospheric sources of NO_x include the oxidation of ammonia (NH_3), and the reaction of $O(^1D)$, which is produced by the photolysis of O_3 in the UVB (280–320 nm) and to a minor extent in the UVA (320–400 nm) with nitrous oxide (N_2O) (Olivier et al., 1994).

In the troposphere, NO_x species participate in the photochemical chain reactions, which oxidize reactive gases, such as volatile organic compounds (VOCs), methane (CH_4), and O_3. Tropospheric O_3 is a greenhouse gas playing an important role in the climate system (IPCC, 2007). NO_x and O_3 are both toxic and the exposure to these hazardous gases impacts on human health, in cities and in the outflow of polluted air from large agglomerations or from outdoor biomass burning (e.g. Künzli et al., 2000; Cancado et al., 2006).

Tropospheric NO_x is primarily removed by the gas phase as nitric acid (HNO_3) during the day and by heterogeneous reactions at night (Wayne et al., 1991). As a result of the pressure dependence of the hydroxyl radical (OH) reaction with NO_2, the lifetime of NO_x is mainly a function of altitude during the day. However, VOCs including isoprene also play an important role in the removal of NO_x, especially when NO_x concentrations are high (Browne and Cohen, 2012). In the lower troposphere, the lifetime of NO_x is relatively short (e.g. Spicer, 1982; Beirle et al., 2011), and as a result, NO_2 is often found close to its sources. Due to the fact that isoprene concentrations over NO_x sources

ACPD
13, 28453–28510, 2013

are still highly uncertain (Guenther et al., 2006), the exact NO_x lifetime is difficult to estimate.

NO_2 amounts and distributions are retrieved from active and passive remote sensing techniques in the ultraviolet (UV)/visible, near infrared (NIR), infrared (IR) and microwave regions of the electromagnetic spectrum. One widely-used technique in the UV/visible is the Differential Optical Absorption Spectroscopy (DOAS) method, introduced by Perner and Platt (1979), which initially was applied to measure tropospheric trace gases, such as NO_2, by active remote sensing using artificial light sources. The key concept of DOAS is the simultaneous fit of several trace gas absorption spectra to the measured atmospheric spectrum using only the high frequency part, whereas the lower frequency spectral structures and scattering features are fitted with a polynomial (Platt and Hausmann, 1994). The invention of Multi AXis (MAX) DOAS allowed the quantification of tropospheric NO_2 by observing scattered sunlight at different viewing directions (Hönninger et al., 2004; Wittrock et al., 2004). An Airborne MAX-DOAS or AMAXDOAS was also subsequently developed (Wang et al., 2005; Heue et al., 2005), and more recently, an imaging DOAS spectrometer (iDOAS) was designed for airborne observations (Heue et al., 2008).

Since the launch of the Global Ozone Monitoring Experiment (GOME) on board ESA's European Remote Sensing (ERS)-2 satellite (Burrows et al., 1999) and the SCanning Imaging Absorption spectroMeter for Atmospheric CHartographY (SCIAMACHY) on board ENVISAT (Burrows et al., 1995; Bovensmann et al., 1999), NO_2 total and tropospheric vertical columns have been retrieved from nadir measurements. The GOME-2 on board the Meteorological Operational (MetOp) satellites is an improved version of GOME (Callies at al., 2004) and was launched in October 2006 (MetOp-A) and in September 2012 (MetOp-B). The Ozone Monitoring Instrument (OMI) on board NASA's Earth Observing System (EOS) Aura satellite, launched in July 2004, is another satellite-based instrument designed for the retrieval of atmospheric trace species (Levelt et al., 2006). In this study, we make use of data from the GOME-2 and OMI in-

ACPD
13, 28453–28510, 2013

struments, which provide information about the NO_2 columns in the morning (GOME-2) and early afternoon (OMI) state of the atmosphere, respectively.

Large vegetation fires, occurring every single month on our planet, emit large amounts of trace species into the atmosphere, among them NO_x. During the combustion process, nitrogen (N) present in the fuel is converted in part into oxides and N present in amino acids is converted to NO. However, NO_x may also result from the reaction of molecular nitrogen (N_2) with O_2 at very high temperatures (Andreae and Merlet, 2001). The atmospheric composition over such biomass burning regions is strongly influenced by the release and subsequent chemical reactions of trace gases (e.g. NO_x, O_3, and VOCs) and aerosols. In spite of the large extent of vegetation fires and their environmental and human health problems, the spatial size and the seasonal variation of these fires were not fully perceived until the late 1970s, as satellite data were not available before. Especially in the main biomass burning regions in the tropics and subtropics, only sparse information existed about fires before the satellite era. During the last decades, however, the amount of space-based information has sharply increased and contributed to a better knowledge of many atmospheric and biospheric processes (Langmann et al., 2009; Ichoku et al., 2012).

The importance of agricultural emissions from biomass burning for air quality was recognized in the 1960s in Europe and elsewhere (Meland and Boubel, 1966). The first global estimates of biomass burning for atmospheric composition were made by Seiler and Crutzen (1980). More recently, it has been estimated that the consumed biomass in the tropics accounts for 80 % of the total biomass burned globally (Crutzen and Andreae, 1990), with Africa and Australia accounting for more than 80 % of the global burned area (Giglio et al., 2006). The estimation of emissions for large areas and long-term periods has to be carried out in a simplified way as the whole combustion process is complex. In the last three decades, different methods were developed for estimating vegetation fire emissions for the entire globe. However, large uncertainties remain with respect to the exact amounts of trace gas emissions, including NO_x, which especially arise from the assumptions made in the various approaches (bottom-

ACPD
13, 28453–28510, 2013

up vs. top-down) and different data sets used in these studies. For instance, top-down emissions of NO_x from biomass burning are estimated at 5.8 Tg NO_x for the year 2000 (Jaeglé et al., 2005). In contrast, recent bottom-up inventories estimated global NO_x emissions from biomass burning at 9.5 Tg $NO_x\,yr^{-1}$ (van der Werf et al., 2010; Kaiser et al., 2012), and thus, there still remain large discrepancies between the results obtained from the bottom-up and top-down approaches. One large source of uncertainties, amongst others, are the emission factors (EFs), which are mainly obtained from extensive laboratory and field measurements (Andreae and Merlet, 2001; Akagi et al., 2011).

Fire radiative power (FRP) is a parameter describing the radiant component of energy release from the fire and is quantified in the IR spectral range (Kaufman et al., 1998). First analyses of satellite-based FRP measurements have indicated clear spatio-temporal differences in the energy radiated by active fires (Wooster and Zhang, 2004). Moreover, Wooster et al. (2005) have found proportionality between FRP and the combustion rate, and thus, proposed a universal conversion factor of 0.368 kg MJ^{-1}, which quantitatively links FRP to dry matter combustion rate. This approach, which substitutes burned area, fuel load, and combustion completeness, and moreover better accounts for the spatio-temporal variability of fires, was taken up again and implemented into the Global Fire Assimilation System (GFASv1.0). GFASv1.0 makes use of biome-specific conversion factors and assimilates daytime and nighttime FRP data for the calculation of the total biomass burned (Kaiser et al., 2012). Although GFASv1.0 is based on a different approach, average annual emissions of NO_x from vegetation fires are in good agreement (±50 %) with the widely used Global Fire Emission Database (GFEDv3.1).

Ichoku and Kaufman (2005) have established a FRP-based method to derive smoke emission rates by using FRP measurements from MODIS on board the polar-orbiting satellites Terra and Aqua. They found differences in the emission strength among different regions and biomes. However, they also pointed out that the derived emission rates are most likely overestimated. Geostationary FRP observations from the Spinning En-

ACPD
13, 28453–28510, 2013

hanced Visible and Infrared Imager (SEVIRI) on board the Meteosat-8 satellite have been used to investigate the annual and diurnal cycle of biomass burning in Africa. It was shown that the diurnal cycles differ markedly among the selected land cover types, but are very similar in both hemispheres. The typical diurnal cycle of FRP is characterized by low fire intensity between 00:00 LT and 07:00 LT, followed by a sharp increase, peaking around 14:00 LT (Roberts et al., 2009). Roberts and Wooster (2008) compared temporally coincident FRP measurements from MODIS and SEVIRI and found strong agreement when both sensors detected a fire successfully. Due to the coarser spatial resolution of SEVIRI, however, the summed FRP is underestimated as the lowest FRP fires are not detected. While MODIS benefits from a higher spatial resolution, it measures only a few times per day, and thus, the temporal integration of FRP is challenging. Freeborn et al. (2011) elaborated on this and combined SEVIRI and MODIS measurements to derive the fire radiative energy (FRE) for the African continent. At the continental scale, FRE estimated by MODIS observations is ~ 30 % less than FRE estimated by MODIS and the additional implementation of SEVIRI measurements, which account for low spatial resolution detection biases. They found that this underestimation is attributed to the MODIS scan geometry and the typical calculation of the sum of FRP.

In this study, the potential of using satellite observed TVC NO_2 for the quantification of NO_x emissions from outdoor biomass burning using a simple statistical approach is evaluated. The temporal correlation of TVC NO_2 and FRP is studied globally and for selected regions. Fire emission rates (FERs) of NO_x (reported as NO) for typical tropical and subtropical biomes are derived for the morning (early afternoon) by making use of the linear relationship between TVC NO_2 from GOME-2 (OMI) and FRP from MODIS on board Terra (Aqua). A similar method to derive smoke emissions rates from FRP measurements was already established by Ichoku and Kaufman (2005), but for aerosols. We follow this concept, present FERs of NO_x for selected tropical and subtropical biomes and regions, and discuss possible factors affecting the biome-specific, diurnal, and regional discrepancies.

ACPD
13, 28453–28510, 2013

The instruments and their associated data retrieval are described in Sect. 2. The results are presented and discussed in Sect. 3, followed by the conclusions and planned future work (see Sect. 4).

2 Instruments and data retrieval

2.1 Satellite measurements of tropospheric NO_2

The second Global Ozone Monitoring Experiment (GOME-2) located on board MetOp-A satellite is the first of a series of three identical instruments which will provide more than 15 yr space-borne UV/visible observations of the atmosphere (Munro et al., 2000). The GOME-like nadir-viewing spectrometer covers the spectral range between 240 and 790 nm at 0.2–0.4 nm resolution, has a ground pixel size of 80 km × 40 km and overpasses the equator at 09:30 LT in the descending node (Callies et al., 2004). With its large swath of 1920 km, GOME-2 provides near global coverage every day.

The Ozone Monitoring Instrument (OMI) on board NASA's EOS-Aura satellite performs spectral measurements in the range of 270–500 nm at a spectral resolution of 0.63 nm (Levelt et al., 2006). In nadir geometry, the instrument overpasses the equator in the ascending node at 13:30 LT with the pixel size being 13 km × 24 km at nadir and larger to the edges of the swath. The OMI instrument provides global coverage of spectral measurements every day.

The retrieval of tropospheric NO_2 vertical columns (TVC NO_2) from the GOME-2 (morning) and OMI (early afternoon) measurements is achieved in four main steps. In the first step, the trace gas concentration integrated along the light path (slant column density or SCD) is determined by applying the Differential Optical Absorption Spectroscopy (DOAS) method, based on Beer–Lambert's law. The DOAS retrieval uses the logarithm of the ratio between Sun- and Earthshine to determine the optical thickness. The differential optical thickness is then determined by the subtraction of a suitable polynomial, and a linear fit of the differential absorption cross-

ACPD
13, 28453–28510, 2013

sections of all absorbers relevant in the spectral region of interest is performed to determine the SCDs. For the GOME-2 instrument, Richter et al. (2011) have developed an improved NO_2 retrieval including more spectral points and an explicit spike removal algorithm by using a larger fitting window (425–497 nm) than used for GOME and SCIAMACHY (425–450 nm). Here, we use SCDs from this retrieval for further analysis. The NO_2 SCDs from OMI were downloaded from the NASA Web site (http://disc.sci.gsfc.nasa.gov/Aura/data-holdings/OMI/omno2_v003.shtml). Details about the DOAS retrieval for the determination of NO_2 SCDs from OMI, which slightly differs with respect to the fitting characteristics, can be found in Bucsela et al. (2006). In the second step, the reference sector method (Richter and Burrows, 2002) is used for removing the stratospheric part from the NO_2 SCDs. The reference sector method simply adducts a region over the Pacific (180–220° longitude), which is assumed to have negligible sources of tropospheric NO_x, and thus, only reflects the stratospheric amount. The stratospheric columns, varying with latitude, are then subtracted from the total columns determined by the DOAS method. For some regions, the subtraction leads to negative values of the tropospheric slant column. This may arise due to zonal inhomogeneities in the stratospheric NO_2 distribution or transport of tropospheric NO_2 into the reference sector, leading to higher values which are then subtracted in remote regions, and thus, result in negative values. While at mid and high latitudes the reference sector method can introduce significant errors (e.g. Hilboll et al., 2013), it is not a concern for the tropical and subtropical regions, which are the focus of this study. Thirdly, measurements with cloud fraction greater than 0.2 are removed via cloud screening by using the improved version of the Fast REtrieval Scheme for Clouds from the Oxygen A-band (FRESCO+) algorithm (Wang et al., 2008). Finally, the tropospheric SCDs are converted into TVC NO_2 by applying airmass factors (AMFs), which are derived from a radiative transfer model (SCIATRAN) by taking into account the viewing geometry and scattering, absorption and reflection within the atmosphere and the Earth's surface. The calculation of AMFs used for this study is based on a priori information of the parameters albedo, ground level, NO_2 vertical profile, and aerosol (optical) proper-

ACPD
13, 28453–28510, 2013

ties. The albedo and ground level information is derived from the GOME albedo data base (Koelemeijer et al., 2003) and the TerrainBase Global DTM Version 1.0 (Row et al., 1994), respectively. The a priori information on the vertical distribution of NO_2 is obtained from the Model for OZone And Related Chemical Tracers (MOZARTv2). The types of aerosols are classified as urban, rural, and maritime. AMF calculations are performed on a horizontal grid of $2.8125^\circ \times 2.8125^\circ$ (according to the resolution of MOZARTv2) for each month of the year 1997. The retrieval is thus using NO_2 profiles which include the effects of biomass burning on a climatological basis but not on a case-by-case basis.

Boersma et al. (2004) have shown that the AMFs are the largest source of error in satellite-based retrievals of tropospheric NO_2. For instance, errors in the CTM-derived NO_2 vertical profile (Hains et al., 2010) and errors in specified aerosol properties (Martin et al., 2003; Leitão et al., 2010) influence the accuracy of AMFs. As aerosols interact with radiation in the atmosphere, AMFs calculated by radiative transfer models are sensitive to optical properties, amount and vertical distribution of aerosols. Martin et al. (2003) found a reduction of AMFs by 10–20 % when influenced by biomass burning aerosols and desert dust. Moreover, an aerosol layer located above the NO_2 concentrations can decrease the AMF by up to 70 % (Leitão et al., 2010). Consequently, the selection of too high (low) AMFs results in an underestimation (overestimation) of TVC NO_2. While the column integrated extinction of aerosols on a global scale is well known (e.g. Remer et al., 2008), further research needs to be carried out to increase the knowledge of vertical profiles of aerosol properties. More information regarding the AMF calculations is found in Nüß (2005) and details concerning the influence of the NO_2 vertical profile and aerosol properties on the AMF are given in Leitão et al. (2010).

The second, third, and fourth steps of the retrieval procedure are performed in the same way for the SCDs from GOME-2 and OMI. Monthly means of TVC NO_2 for the five consecutive years (2007–2011) are binned to a horizontal resolution of $1^\circ \times 1^\circ$.

ACPD
13, 28453–28510, 2013

2.2 Satellite measurements of fire radiative power

The MODerate resolution Imaging Spectroradiometers (MODIS) on board NASA's Terra and Aqua satellites were launched in sun-synchronous near-polar orbits in December 1999 and May 2002 with corresponding equatorial overpass times at 10:30 LT and 13:30 LT, respectively. The instruments were designed to improve the understanding of processes on land, in the oceans, and in the atmosphere. The instruments have 36 spectral bands ranging in wavelength from 0.4–14.4 µm. The differences in 4 and 11 µm black body radiation emitted at combustion temperatures are used to derive active fires at 1 km^2 horizontal resolution. In addition to the binary fire flag, the MOD14 (MODIS Terra) and MYD14 (MODIS Aqua) fire products offer the radiant component of energy release, the so-called fire radiative power (FRP) (Kaufman et al., 1998; Justice et al., 2002). FRP is described by the Stefan–Boltzmann law, which characterizes the power radiated from a black body in terms of its temperature. Riggan et al. (2004) have found that more than 90 % of the radiant energy released by vegetation fires was observed between 830 K and 1440 K with the flaming (smoldering) temperature sometimes exceeding (undershooting) 1600 K (700 K). Although there is a lack of validation concerning the satellite-derived parameter FRP, and studies dealing with FRP are rather new, recent studies have tried to assess the uncertainties in FRP. For instance, Schroeder et al. (2010) found that the detection limits are 11 and 9 MW for MODIS on board Terra and Aqua, respectively, over the Brazilian Amazon. Coincident space-based observations of the Geostationary Operational Environmental Satellite (GOES) indicated increased detection limits of 27 and 19 MW during Terra and Aqua overpass time, respectively. Due to the larger amount of non-detected (smaller) fires, SEVIRI and GOES derived FRP is underestimated by 40–50 %, when compared to FRP from MODIS (Roberts and Wooster, 2008; Xu et al., 2010). Monthly data of FRP for the consecutive five years (2007–2011) have been downloaded at a horizontal resolution of 1° × 1° from ftp://neespi.gsfc.nasa.gov/data/s4pa/Fire/.

ACPD
13, 28453–28510, 2013

2.3 Global land cover map

The Collection 5 MODIS Global Land Cover Type product, which is generated at a horizontal resolution of 500 m, was designed to support scientific investigations (Friedl et al., 2010). The MODIS land cover product is based on five different classification systems and freely available at https://lpdaac.usgs.gov/products/modis_products_table/mcd12q1. The map used for this study represents the 2005 land cover types and has been spatially aggregated to a $1^\circ \times 1^\circ$ resolution using a majority filter, which selects the most abundant land cover type within the $1^\circ \times 1^\circ$ pixel. Among the different classifications included in this product, we have selected the 14-class University of Maryland classification (UMD), which includes the land cover types evergreen broadleaf forest, open shrublands, woody savannas, savannas, and croplands (Hansen et al., 2000).

2.4 Satellite measurements of aerosol optical depth

The collection 5 MODIS aerosol products are derived from spectral radiances between 470 and 2130 nm and provide a consistent record of aerosol characteristics (Remer et al., 2008). The column integrated extinction, commonly referred to as aerosol optical depth (AOD), is a straightforward space-based parameter for characterizing the Earth's aerosol system. As aerosols can significantly influence the AMFs used for the retrieval of TVC NO_2 from satellite measurements (e.g. Martin et al., 2003; Leitão et al., 2010; Bousserez, 2013), we use AOD measurements at 550 nm from MODIS on board Terra and Aqua and investigate the temporal relationship between AOD and FRP over the selected regions. In general it is expected, that AOD is highly correlated with FRP where biomass burning is the main aerosol source. This information might be useful to discuss the possible impact of aerosols on the estimated FERs of NO_x (see Sect. 3.5). The AOD product has been downloaded at a $1^\circ \times 1^\circ$ horizontal resolution from ftp://ladsweb.nascom.nasa.gov/allData/51/MOD08_M3/2005/.

ACPD
13, 28453–28510, 2013

2.5 Population density

Population density has been inferred from the Global Rural–Urban Mapping Project (GRUMPv1) in order to separate pixels which are largely influenced by anthropogenic emissions, resulting from fuel combustion in energy production and transportation. GRUMPv1 builds on the Gridded Population World (GPW) project to construct a common geo-referenced framework of urban and rural areas by combining census data with satellite data. The actual version of GRUMP consists of three data products. One important part of GRUMPv1 is a higher resolution population dataset at a $30'' \times 30''$ grid for the years 1990, 1995, and 2000, with the latter one being used for this study. The second component of GRUMPv1 is based on NOAA's night-time lights data. Beyond that, GRUMPv1 allocates a point data set of all urban areas with populations of greater than 1000 persons. The population density grid data set used for this study is available at http://sedac.ciesin.columbia.edu/data/collection/gpw-v3. According to the TVC NO_2, FRP, AOD, and the global land cover map, the population density map has been gridded to a $1^\circ \times 1^\circ$ horizontal resolution.

2.6 Conversion of tropospheric NO_2 vertical columns into production rates of NO_x

The reason for the conversion of tropospheric NO_2 vertical columns into production rates of NO_x is twofold: as chemical models typically require values for the amount of NO_x being released as a function of time, we estimate the monthly mean top-down production rate of NO_x from fire (P_f) for five consecutive years of GOME-2 and OMI measurements (2007–2011), and thus, provide P_f (in $g\,NO_x\,s^{-1}\,pixel^{-1}$) for the morning and early afternoon, respectively, according to the local overpass time of the two satellites. Another reason for the conversion is to enable comparability between TVC NO_2 and values of existing bottom-up emission inventories for biomass burning, e.g. GFEDv3.1. According to the units reported in GFEDv3.1 (in $g\,NO_x\,month^{-1}\,m^{-2}$), P_f is temporally integrated over a month.

ACPD
13, 28453–28510, 2013

As previously stated, the tropospheric NO_2 vertical column is determined as:

$$TVC = \int [NO_2](z)dz, \quad (1)$$

where $[NO_2](z)$ is the concentration of NO_2 at altitude z of the atmosphere, integrated from the ground to the tropopause.

The instantaneous change in NO_2 is given by:

$$\frac{d[NO_2]i}{dt} = P - L[NO_2]i, \quad (2)$$

where t is the time, P is the production rate of NO_2 and L is the loss rate of NO_2. The loss rate is given by:

$$L = [NO_2]i \sum jk(ktix + ktiy + kb)(Xj + NO_2)j[xi] + kter(Yk + NO_2 + M), \quad (3)$$

where ktx, kty and ktz are transport rate coefficients for x, y, and z directions, respectively, and:

$$ktix = 1/tix, \quad ktiy = 1/tiy, \quad ktiz = 1/tiz, \quad (4)$$

where for altitude level i, tix, tiy, and tiz are the time constants for the transport out of the field of view in the x, y, and z directions, respectively.

While the term $kb(Xj + NO_2)j$ represents the rate coefficients for the bimolecular reaction of NO_2 with Xj, the term $kter(Yk + NO_2 + M)$ is the termolecular rate coefficient for the reaction of NO_2 with Yk and a third body.

For point sources like megacities, Beirle et al. (2011) assume that the decay of NO_2 in the outflow can be fitted by a first order decay constant. They typically found time constants for the decay of NO_2 ranging from 4–8 h during daytime, with the shortest lifetimes (τ) derived for lower latitudes. Following these findings, we neglect the above stated Eqs. (2)–(4) and simply assume a constant lifetime of NO_2 of the order of $\tau = 6$ h

ACPD
13, 28453–28510, 2013

for both the morning and early afternoon state of the troposphere. As a consequence of the still poorly understood local concentrations of VOCs, which play an important role in the removal of NO_x, and thus, affect the lifetime of NO_x, we argue that this assumption is adequate for the focus of this study. We cannot expect better results for the lifetime of NO_x retrieved from chemical models, as long as the concentrations of VOCs over biomass burning regions are not accurately known.

If NO_2 columns are averaged over larger pixels, e.g. $1^\circ \times 1^\circ$ pixels, the effect of advection in and out of the region can be neglected and the change of NO_2 columns is dominated by chemistry. The instantaneous stationary state of NO_2 can then be described as:

$$\frac{\mathrm{d}[NO_2]i}{\mathrm{d}t} = P - L[NO_2]i = 0 \rightarrow P = L[NO_2]i \quad (5)$$

In the case of fire, we assume that P is dominated by the fire release and that it is negligible on days where no fires occur within the pixel. Typically, chemical models require values for the amount of NO_x being released as a function of time and area. Assuming that (i) FRP is a surrogate for the fire temperature, (ii) NO or NO_x is produced instantaneously, and (iii) the NO_2/NO_x ratio in the plume is defined by the Leighton photostationary state (Leighton, 1961):

$$\frac{[NO_2]i}{[NO]i} = \frac{k1[O_3]i}{J2i}, \quad (6)$$

we determine P for the photolysis frequency of NO_2 ($J2i$), meaning for the time and therefore solar zenith angle of the GOME-2 (morning) and OMI (early afternoon) overpass. Instead of inferring the rate constant for the reaction of ozone with NO ($k1$) and tropospheric O_3 concentrations from climatologies, we follow the findings of Alvarado and Prinn et al., (2009) and assume a constant $[NO_2]/[NO_x]$ ratio of 0.75. In order to convert the satellite-derived NO_2 amounts produced by fire (TVC_f NO_2) for the comparison with fire NO_x emissions from GFEDv3.1, the background levels of tropospheric

ACPD
13, 28453–28510, 2013

NO_2 (TVC_b NO_2) are subtracted from TVC NO_2 as a first step.

$$TVC_f[NO_2] = TVC[NO_2] - TVC_b[NO_2] \quad (7)$$

The background values of NO_2, also referred to as *y*-intercepts, are taken from the analysis of the least-squares method for the subtraction (see Sect. 3.2 and Fig. 5).

The estimation of P_f is based on the conversion between the column number density (in molecules cm^{-2}), as retrieved from satellite instruments, into column mass concentration (in $g\,cm^{-2}$). This part of the approach requires Avogadro's number (N_A) and the molar mass (M) of NO, as the emissions of NO_x are reported as NO in state-of-the-art emission inventories. The molar mass of NO is $30\,g\,mol^{-1}$. The following equation summarizes the above stated approach for estimating P_f (in $g\,NO_x\,s^{-1}\,pixel^{-1}$) for a single $1^\circ \times 1^\circ$ box:

$$P_f = \frac{TVC_f[NO_2] \cdot M \left(1 + \frac{NO}{NO_2}\right) A_p}{N_A \cdot \tau}, \quad (8)$$

where TVC_f NO_2 is the number density of NO_2 molecules produced by fires and integrated over the tropospheric vertical column (in molecules cm^{-2}), M is the molar mass of NO (in $g\,mol^{-1}$), A_p is the respective pixel area (in cm^2), and N_A determines Avogadro's number (in molecules mol^{-1}). The term $1 + NO/NO_2$ accounts for the above stated ratio (without units), and τ is the lifetime of NO_x (in seconds). According to the described conversion of TVC NO_2, the FRP values have also been multiplied by A_p. As described earlier, P_f is multiplied by the number of seconds per month for the comparison with GFEDv3.1 NO_x (in $g\,NO_x\,month^{-1}\,m^{-2}$).

Our approach to derive space-based FERs of NO_x is based on the relationship between the above described parameters P_f and FRP. It is important to note that the retrieval of TVC NO_2 is based on static AMFs. Consequently, biome-specific, diurnal, and regional discrepancies in FERs of NO_x could be affected by changes in the NO_2 vertical profile and aerosol properties relative to the a-priori. The conversion of TVC

ACPD
13, 28453–28510, 2013

NO_2 into P_f further assumes constant values for the lifetime of NO_x and the NO_2/NO_x ratio. Therefore, biome-specific, diurnal, and regional variations in FERs could also be influenced by changes in plume chemistry.

3 Results and discussion

The aim of this study is to establish an empirical relationship between tropospheric NO_2 vertical column (TVC NO_2) and fire radiative power (FRP) as a tool to estimate fire emissions of NO_x. For this purpose, we derive the gradient of the linear relationship between the converted TVC NO_2, here referred to as production rate of NO_x from fire (P_f), and FRP over characteristic tropical and subtropical biomass burning regions. The gradients, here referred to as FERs of NO_x, for the morning (early afternoon) fires are obtained from the relationship between P_f, retrieved from GOME-2 (OMI) and converted according to Eqs. (7) and (8), and FRP, retrieved from MODIS on board Terra (Aqua). A global grid with a horizontal resolution of $1^\circ \times 1^\circ$ for a total of five different types of vegetation is used and evaluated for these regions.

In a first step, monthly means of TVC NO_2 are analyzed for their temporal correlation with monthly means of FRP for five consecutive years from 2007 to 2011 on a $1^\circ \times 1^\circ$ grid. Secondly, we determine spatially averaged regression coefficients for the selected regions. The obtained regression coefficients are then used for the prediction of tropospheric NO_2 columns by simply applying a linear regression model. Thirdly, we compare the production rate of NO_x from fire as derived from GOME-2 and OMI measurements with the GFEDv3.1 NO_x. In order to ensure comparability of the obtained FERs in this study with the fire emissions of NO_x typically found in the state-of-the-art emission inventories, we convert the number density of the NO_2 columns into mass concentrations of NO_x (see Sect. 2.6). In a fourth step, we derive FERs for different types of vegetation on a $1^\circ \times 1^\circ$ grid by using a global land cover map and filtering the data based on population density. Finally, we discuss possible factors that could

ACPD
13, 28453–28510, 2013

affect the retrieval and conversion of TVC NO_2 and P_f, and thus, the magnitude of the presented FERs of NO_x.

3.1 Correlation between tropospheric NO_2 and fire radiative power

The global distribution of TVC NO_2, averaged over five consecutive years (2007–2011), is shown in Fig. 1, indicating that the natural sources and emissions of NO_x are much more equally distributed over the Earth's surface and in the atmosphere than anthropogenic sources and emissions. We note that the upper limit of TVC NO_2 is restricted to 5×10^{15} molec cm^{-2}, in order to differentiate between the NO_2 production from anthropogenic and natural sources. The clear spatio-temporal variations of TVC NO_2 result from the inhomogeneous distribution of its sources and the relatively short lifetime of NO_x, which is estimated to be in the order of hours (e.g. Beirle et al., 2011). Moreover, it is obvious that the order of magnitude of the averaged TVC NO_2 is smaller for biomass burning regions (e.g. in Africa, north and south of the equator) than for large agglomerations (e.g. central east China). Nevertheless, the release of NO_x emissions observed in these biomass burning regions influences the atmosphere on a large scale, and thus, accurate NO_x emission estimates from vegetation fires are needed. For further analysis, we have selected five characteristic biomass burning regions which are highlighted and defined in Fig. 1 and Table 1.

A previous study by Giglio et al. (2010) showed that the total yearly area burned in these five regions accounts for about 85 % of the total global area burned on average. In some years, more than 10 % of the total continental area is burned in Africa. These findings support the selection of these regions, as most of the global fire activity and its resulting emissions of trace gases and aerosols are observed within their boundaries. Moreover, it is clear that the selected regions are generally far away from megacities, which produce significant amounts of NO_x by high temperature combustion processes, except for Southeast Asia (SEA).

The temporal correlation coefficients for each $1^\circ \times 1^\circ$ pixel are calculated from the consecutive five year data sets of TVC NO_2 and FRP (see Fig. 2). The morning obser-

ACPD
13, 28453–28510, 2013

vations (GOME-2 TVC NO_2 vs. MODIS Terra FRP) show that the highest correlation coefficients of $r > 0.8$ are found in Africa, south of the equator (ASE) and Africa, north of the equator (ANE). Moderate to high correlation coefficients are also apparent in central South America (CSA), northern Australia (NAU), and SEA. Temporal correlation between TVC NO_2 and FRP is also found beyond 30° N and 30° S, especially in boreal ecosystems, but much less strong and widespread. This is probably due to the lower signals in TVC NO_2 and FRP data sets and due to much less pronounced seasonal variations of the aforementioned parameters. The negative correlation coefficients over large agglomerations can be explained as a consequence of higher NO_2 levels being observed in the wintertime, whereas NO_x emissions from vegetation fires (mainly cropland fires) in the summertime are much lower in magnitude. However, these regions with negative correlation are not included for the estimation of the FERs (see below). The spatial distribution and magnitude of the correlation coefficients obtained from the relationship between TVC NO_2 and FRP for the early afternoon (OMI vs. MODIS Aqua) is in good agreement with the morning correlations shown in Fig. 2 (not shown here), underlining the robust link between TVC NO_2 and FRP.

Figure 3 illustrates the time series of monthly means of TVC NO_2 and FRP, averaged over the selected regions, for the morning (GOME-2 vs. MODIS Terra) and early afternoon (OMI vs. MODIS Aqua) observations. In the case of TVC NO_2, 1° × 1° boxes located over the open ocean are included in the averaging procedure. While the inclusion of these pixels reduces the magnitude of the monthly mean TVC NO_2 and FRP values, especially in ANE, we expect no deterioration of the overall seasonal variation. The seasonal variability of FRP, which peaks during the dry season, is reflected by the NO_2 measurements to a high degree, especially in ANE, ASE, and CSA. The high consistency between the two seasonal cycles is a consequence of the relatively short lifetime of NO_x and the resulting small horizontal transport.

Biomass burning as a dominant NO_x emission source in tropical regions was already mentioned by Cahoon et al. (1992). Moreover, the seasonal variation of NO_2 for African biomass burning regions, usually peaking during the dry season, was pointed out by

ACPD
13, 28453–28510, 2013

van der A et al. (2008). They used a simple classification scheme for the identification of NO_x sources based on seasonality and showed that the movement of maximum NO_2 concentrations correlated well with fire count observations from the AVHRR and the ATSR satellite-based instruments.

In contrast to the African regions and CSA, the agreement between TVC NO_2 and FRP in our study is weaker over NAU and SEA. As the influence of anthropogenic sources in the selected regions remains low when spatially averaged (except for SEA), the enhanced dry season tropospheric NO_2 levels are mainly produced by active fires. In the wet season, tropospheric NO_2 levels result from soil microbial activity, lightning, and high temperature combustion processes induced by humans (e.g. Beirle et al., 2004). Indeed, the interannual variability of TVC NO_2 over ANE and ASE is less apparent during the dry season (maxima) than during the wet season (minima). This fact indicates an overall uniform interannual pattern of fire activity, which is dominated by the controlled slash and burn practices (Fig. 3).

In general, the early afternoon observations indicate higher intensity in fire, and thus, higher values of TVC NO_2. This feature has already been found over tropical regions in a previous study by Boersma et al. (2008). They showed that column mixing ratios of NO_2, detected by OMI (13:30 LT), are typically more than 40 % higher than mixing ratios detected by SCIAMACHY (10:00 LT). However, in CSA there are no significant differences between morning and early afternoon signal of TVC NO_2, although the intensity of fires is much higher during early afternoon. Possible explanations could be the differences in the detection sensitivity of fires or diurnal changes in the removal of NO_x. Another interesting feature is observed over NAU, as there are only minor differences between morning and early afternoon observations for both TVC NO_2 and FRP. In contrast to the usual diurnal cycle of fire intensity observed in other regions, which steeply increases in the early afternoon elsewhere, the fire intensity in NAU is even lower during the OMI overpass than during the GOME-2 overpass. This feature is also found in Fig. 3, where no obvious differences between the morning and early afternoon fire intensity are visible. In contrast, the differences of TVC NO_2 and FRP

ACPD
13, 28453–28510, 2013

between morning and early afternoon are more distinct in the African regions. We suggest that the impact of accumulating NO_2 concentrations in these regions is stronger than changes in NO_x lifetime between morning and early afternoon.

The highest spatio-temporal averaged FRP, derived from the morning observations, occurred in October 2011 in NAU, which is however an exception, as the usual observed monthly FRP is two times smaller. One explanation for these unusually high values in NAU could be the strong rainfalls in early 2011, which lead to higher amounts of fuel available for the burning later in the dry season. Overall, the early afternoon observations of FRP show that the highest spatio-temporal means are found over ASE and CSA (see Fig. 3).

As already mentioned before, the lower mean values of TVC NO_2 in ANE can be explained by the fact that more $1^\circ \times 1^\circ$ boxes with low values of TVC NO_2 over the ocean are included in the averaging procedure. As a consequence of the higher background levels of tropospheric NO_2, the seasonal variability of TVC NO_2 is less pronounced in SEA. Moreover, the higher values of TVC NO_2 retrieved from GOME-2 most likely arise from the higher emissions of NO_x in the morning rush hours in larger agglomerations located in this region.

3.2 Determination of regression coefficients

We have computed area-averaged regression coefficients for the morning and early afternoon and the selected regions (see Fig. 4) for generating simple linear regression models. In general, the obtained gradients show good agreement among the regions with the highest gradients being observed in the early afternoon over the African regions. While the morning and early afternoon gradients over NAU and SEA show a similar rise, obvious differences in gradients are observed in CSA. The computed *y*-intercepts show some degree of disagreement among the regions, especially between those calculated for the African regions and CSA.

The higher background levels in ANE and ASE (compared to CSA) may arise from the higher wet season emission rates of savanna soils dominating in these regions.

ACPD
13, 28453–28510, 2013

This is in good agreement with the findings of Yienger and Levy (1995), as they suggest much lower emission rates of NO_x from soil microbial activity in tropical rain forests covering large areas in CSA. Meyer-Arnek et al. (2005) have shown that a significant amount of TVC NO_2 could also be attributed to NO_2 production from lightning, as the lifetime of NO_2 is longer in the upper troposphere. In comparison to the dry season peak values of TVC NO_2 and FRP, the wet season values within ANE, ASE, CSA, and NAU are about two thirds smaller in magnitude.

The spatial distribution of *y*-intercepts and gradients, based on the best fitting least-squares regression lines, is shown in Figs. 5 and 6, respectively. The higher (lower) gradients indicate that lower (higher) values of FRP are necessary for reaching a specific NO_2 level. The distribution of the gradients is smooth and shows only moderate variation, indicating that a robust link exists between TVC NO_2 and FRP (Fig. 6). In contrast, the values of the calculated *y*-intercepts show much more heterogeneity among the selected regions (Fig. 5).

For instance, high *y*-intercepts in ANE are found in the coastal region of Nigeria, which is one of the world's most densely populated regions with many well-known emission sources from oil mining and gas flares (e.g. Marais et al., 2012). The Greater Bangkok area in SEA, which is influenced by many emission sources, such as high-traffic roads, is also characterized by high *y*-intercepts. For instance, the emissions from public and private cars in Bangkok are estimated to contribute up to 80 % of NO_x (Sahu et al., 2011). Both cases can be interpreted as a clear signal of anthropogenic sources increasing the tropospheric NO_2 columns. On the other hand, low *y*-intercepts represent rather remote areas without any anthropogenic influence, as observed over northern parts of Australia (see Fig. 5).

As a test of how good the assumption is that the observed TVC NO_2 is dominated by biomass burning emissions, monthly area-averaged regression coefficients calculated for the individual regions are used in a simple linear model to predict satellite NO_2 columns using FRP (see Fig. 7). As was expected from the high temporal correlation indicated in Figs. 2 and 4, the tropospheric NO_2 columns can be reproduced by simply

ACPD
13, 28453–28510, 2013

applying regression coefficients and monthly means of FRP. The agreement between observed and estimated NO_2 columns is best for ANE (±40 %) and ASE (±40 %). Larger differences in the order of 100 % are observed for CSA, NAU, and SEA. However, it is clear that large fractions of the NO_2 signal are explained by the seasonal variation of FRP. The overall agreement between the observed and calculated TVC NO_2 for the early afternoon is similar (not shown here).

3.3 Comparison between P_f and GFEDv3.1 NO_x

The estimates of NO_x emissions found in biomass burning emission inventories based on the bottom-up approach, such as GFEDv3.1 (van der Werf et al., 2010), are usually given as g $NO_x\,m^{-2}\,month^{-1}$. In order to compare the values from the emission inventory with TVC NO_2 retrieved from GOME-2 and OMI measurements, the production rate of NO_x from fire (P_f) has to be determined (see Sect. 2.6). According to the units reported in GFEDv3.1, we have converted the column number density of NO_2 (in molecules cm^{-2}), as retrieved from GOME-2 and OMI measurements, into mass concentrations of NO_x produced by fires (in g $NO_x\,m^{-2}\,month^{-1}$).

The scatter plots of P_f obtained in this study vs. GFEDv3.1 are shown in Fig. 8 for the selected regions. While the blue line represents the correlation between P_f obtained from GOME-2 measurements and GFEDv3.1 NO_x, the red line shows P_f obtained from OMI against GFEDv3.1 NO_x. There is a clear correlation between the two parameters with the best agreement found for the African regions. In these regions, we found a stronger gradient for the early afternoon observations, which is related to the fact that the fire intensity in the early afternoon is higher (see Figs. 3 and 4). Consequently, higher fire intensity increases the release of NO_x emissions. A similar pattern is also found for CSA and SEA, where P_f calculated from GOME-2 is lower than P_f calculated from OMI. However, the observed differences are smallest for NAU, possibly due to the small differences in fire intensity between morning and early afternoon, as addressed in Sect. 3.1. Giglio (2007) found a bimodal diurnal cycle in fire activity in northern Australia peaking around 11:00 LT and 16:00 LT. The decrease in fire activity

ACPD
13, 28453–28510, 2013

between 11:00 LT and 13:30 LT (OMI equatorial overpass time) could explain these low observed discrepancies. By estimating the time expressing the average of daily fire activity from the findings of Giglio (2007) and Roberts et al. (2009), we found that it generally occurs between 09:30 LT and 13:30 LT. According to this estimation, the blue (red) lines are expected to have a lower (higher) slope than the 1 : 1 lines. However, in most of the regions, both slopes are lower than the 1 : 1 lines, suggesting that the either GFEDv3.1 NO_x is overestimated or P_f from GOME-2 and OMI is underestimated.

3.4 Fire emission rates of NO_x for selected biomes and regions

As there is some indication of heterogeneity in the global map of mean gradients, shown in Fig. 6, the inclusion of a global land cover map (Fig. 9) and a population density data set (not shown here) is a next step towards understanding these differences and estimating the FERs of NO_x. We use a $1^\circ \times 1^\circ$ gridded global land cover map with a total of five types of vegetation (see Fig. 9) to compute the FERs for the dominating biomes within the five selected regions. For deriving the FERs, the best fitting least-squares regression lines between P_f and FRP are computed for each land cover type using all $1^\circ \times 1^\circ$ pixels having $r > 0.3$ (see Fig. 2). Additionally, the population density of GRUMPv1 is used in the algorithm for the exclusion of strongly anthropogenically influenced (mainly by the residential and industrial sectors) $1^\circ \times 1^\circ$ boxes, using a threshold value of 100 persons km^{-2}. The calculations have been performed for the GOME-2 vs. MODIS Terra (morning) and OMI vs. MODIS Aqua (early afternoon) observations.

Table 2 lists the land cover types with their region-specific absolute numbers of $1^\circ \times 1^\circ$ boxes included in the analysis, where morning and early afternoon numbers are shown on the left and right, respectively. The FERs have then been obtained for each land cover type, when the absolute number is higher than 500. Due to the large number of P_f and FRP values, derived from the consecutive five years data sets, we use a binning method for averaging these values over a successive FRP-interval of 15 MW pixel^{-1}. To ensure the quality, the averaging procedure only includes intervals, where the number of values exceeds 25 within the interval. We note that this averaging procedure is also

ACPD
13, 28453–28510, 2013

intended to reduce the deterioration of the linear relationship by the influence of a few very large fire events which, however, produce unexpected low levels of tropospheric NO_x. For instance, there is a clear signal of a non-linear relationship between P_f and FRP for savannas beyond 800 MW pixel^{-1} in ANE (see Fig. 10). However, it is also clear that these single fire events are rather few when compared to the overall fire activity in this region.

A summary of the derived biome-specific FERs for the selected regions ANE, ASE, CSA, NAU, and SEA is given in Fig. 11 and Table 3. As already mentioned above, we have implemented a threshold value of 500 for the absolute number of pixels included after filtering the data according to population density and correlation coefficient. Therefore, the calculations of FERs within the boundaries of the selected regions have also been restricted to the rather frequently burned land cover types, such as evergreen broadleaf forest, open shrublands, woody savannas, savannas, and croplands. The estimated FERs of NO_x for the dominating types of vegetation burned are lowest for open shrublands (0.33–0.34 g NO_x s^{-1} MW^{-1}) and savannas (0.28–1.03 g NO_x s^{-1} MW^{-1}) and highest for croplands (0.87–1.56 g NO_x s^{-1} MW^{-1}) and woody savannas (0.82–1.54 g NO_x s^{-1} MW^{-1}). The FERs of NO_x are generally larger in the African regions than elsewhere, except for croplands where highest values are found in SEA.

In a recent study by Mebust et al. (2011), OMI NO_2 data for a smaller region in California and Nevada were used together with detailed meteorological information and a high resolution (500 m × 500 m) land classification to estimate biomass burning emission coefficients (ECs). Concerning the geographical location, vegetation, and climate, their selected region is in best agreement with NAU investigated in this study. The results of Mebust et al. (2011), which are based on a similar approach, show higher values for open shrublands (shrubs). For the other two land cover types (forests and grasslands), a comparison is difficult, as grasslands and extratropical forests are not included in our analysis. In a more recent study by Mebust and Cohen (2013), smaller modifications were made to the approach and ECs were calculated for different biomes

ACPD
13, 28453–28510, 2013

on a global scale. In general, they found the highest values for grasslands (including savannas and woody savannas), which is in good agreement with the values derived in our study. However, the magnitude of the ECs in their study is about two times smaller than the magnitude of FERs obtained in our study.

A regional comparison shows that the FERs for woody savannas and savannas in ANE, ASE, CSA, and SEA are similar, whereas the FERs are significantly lower in NAU than elsewhere. One explanation could be the differences in plant characteristics in various regions or even on different continents. For instance, the *N* content in the fuel of savannas could be higher in the African regions than in Australia, and thus, higher amounts of TVC NO_2 are reached by the same intensity of FRP. Mebust and Cohen (2013) argue that the fuel moisture could also play a significant role, as they found a significant cycle in fire emission rates of NO_x for the African woody savannas. From their point of view, this means that the African regions experience an overall drier season, and thus, the FERs are higher due to the fact that the *N* content in the fuel is likely more efficiently converted into NO_x.

We have converted the FERs into emission factors (EFs), in order to compare our obtained results with the EFs found in the literature and frequently used for the estimation of NO_x emissions from outdoor biomass burning via the bottom-up approach. Following the approach by Wooster et al. (2005) who suggested a constant conversion factor of 0.368 $kg\,MJ^{-1}$ for linking the FRP to the dry matter combustion rate, 2.717 MJ of fire energy are needed for the combustion of one kg dry matter. This factor could be directly applied for the translation of the obtained FERs into EFs of NO_x. However, a more recent study by Kaiser et al. (2012) has shown that this constant value is probably not valid for different types of vegetation under realistic wild fire conditions. We therefore make use of the conversion factors provided in their study for different land cover types and apply them for the conversion of FERs into EFs. Here, we use averages of the suggested conversion factors, as they are listed with and without organic soils.

ACPD
13, 28453–28510, 2013

The comparison of the EFs estimated in our study with EFs found in the emission factor compilations by Andreae and Merlet (2001) and Akagi et al. (2011) demonstrates partial agreement (Table 4). The EFs for evergreen broadleaf forest (tropical forest) estimated in the present study are 2–3 times smaller than the one suggested by Andreae and Merlet (2001) and Akagi et al. (2011). We found a better agreement with the two studies for woody savannas and savannas (savanna and grassland). One possible reason for the lower values found for evergreen broadleaf forest could be an overestimation of the NO_x lifetime over these tropical forests. As discussed above, the elevated VOC concentrations over such biomes enhance the removal of NO_x. In general, the EFs for woody savannas and savannas are slightly lower when compared to the EFs found in the literature. Lower values of EFs for savanna and grassland were also pointed out by Martin et al. (2003) and Inness et al. (2013). The authors of the latter study have indicated discrepancies between their reanalysis of TVC NO_2 and TVC NO_2 retrieved from SCIAMACHY for the African regions. They relate the overestimation of their NO_2 reanalysis data to the use of too large EFs for the translation of biomass burned into emissions of NO_x. At this point, we find that the large discrepancies between bottom-up and top-down fire emission estimates of NO_x might be related to these large differences in EFs found for woody savannas (savanna), which is one of the most frequently burned land cover type in Africa. Overall, we found the highest EFs for cultivated crops, being 1.5–2.5 times higher than the one suggested by Andreae and Merlet (2001) and Akagi et al. (2011).

It should be mentioned that both the EFs derived from laboratory and outdoor measurements as well as the EFs estimated in our study are associated with uncertainties. For instance, laboratory studies do not account for the seasonal variability of EFs, which is known to depend on the weather conditions and the connected moisture content in the fuel. The decreasing fuel moisture in Southern African savanna throughout the dry season was shown to have a significant impact on the EFs obtained for different trace gases (Korontzi et al., 2003). Recently, Mebust and Cohen (2013) considered a second possible mechanism for the seasonal variation in EFs. They argue that

ACPD
13, 28453–28510, 2013

a possible reason for the drop of TVC NO_2 over the fire season could be related to the decreasing *N* content in the fuel throughout the dry season. In our approach, such temporal changes in emission fluxes are averaged out by applying a least-squares fit and a binning method.

3.5 Possible factors affecting the magnitude of FERs of NO_x

As discussed in the previous sections, there are interesting differences and patterns in the FERs calculated in this study. However, there are also uncertainties in the approach taken which could affect some of the results and will be discussed in the following.

First of all, tropospheric NO_2 columns over tropical and subtropical biomass burning regions have uncertainties of up to 30 %, as discussed in the extensive error analysis for satellite-based retrievals of TVC NO_2 by Boersma et al. (2004). In a more recent study by Bousserez (2013) it was pointed out that the uncertainties might even be larger (up to 60 %) as the influence of an elevated aerosol layer developing during Harmattan fronts can have a negative aerosol impact on the AMF. The use of spatio-temporal averages of TVC NO_2, as performed in our study, probably leads to a decrease in uncertainties reported above. Using the y-intercept of the regression between TVC NO_2 and FRP for determining the background TVC_b assumes that NO_x emissions from other sources do not have a seasonality which is not correct and can introduce uncertainties of up to 20 %, depending on the region. In addition to the uncertainties arising during the satellite-based retrieval procedure, the conversion of TVC NO_2 into production rates of NO_x from fires contributes to the uncertainty in the estimated FERs. This includes the assumption of a constant lifetime of NO_x (τ = 6 h) as wells as a constant NO_2/NO_x ratio (0.75) for estimating the production rate of NO_x, where both quantities depend on altitude, atmospheric composition, time of day, and probably also on the type of fire. This uncertainty is difficult to assess but could be as large as 30 %. However, the estimated production rates of NO_x are consistent to some degree with the emission fields of NO_x from GFEDv3.1, and thus, the rough assumptions made for the NO_2/NO_x ratio and the lifetime of NO_x seem to work well for the given approach. Retrieving the sum of

ACPD
13, 28453–28510, 2013

FRP by applying the typical calculation can also introduce a negative bias in the order of 30 % (Freeborn et al., 2011). Due to the fact that the errors in both TVC NO_2 and FRP have a rather negative direction, the overall uncertainties of FERs are reduced.

As outlined above, we use static AMFs as well as constant values for the NO_x lifetime and the NO_2/NO_x ratio for the retrieval of TVC NO_2 and the conversion into P_f. Therefore, the FERs and EFs derived in this study could be affected by errors arising from biome-specific, diurnal, and regional changes in AMFs, NO_x lifetime, and NO_2/NO ratio. One possible source of errors is unaccounted for diurnal changes in the boundary layer height, which has a tendency to increase between GOME-2 and OMI overpasses. The effect of an overestimated boundary layer height is twofold: first, the measurement sensitivity, which is smaller close to the surface, is underestimated, and consequently, the AMF is overestimated (Leitão et al., 2010). Second, the lifetime of NO_x, which during daytime is mainly a function of the altitude, could be overestimated. Other possible sources of errors are related to diurnal changes in aerosol properties. For instance, a decrease in the single scattering albedo (SSA) due to an increase of the combustion efficiency between morning and early afternoon can result in a general decrease of the AMF. This effect is especially pronounced in more polluted atmospheres with an increased AOD. In our analysis, the NO_x lifetime is assumed to be constant. However, a decrease or increase in NO_x lifetime between GOME-2 and OMI overpasses could also contribute to the overall error. We note that all of these possible error sources could also partially affect the observed regional differences in FERs.

Concerning the diurnal discrepancies in FERs of NO_x (by comparing morning and early afternoon FERs), we find that FERs for evergreen broadleaf forest are about 20 % lower in the early afternoon in ANE, CSA, and SEA (see Table 3). In general, diurnal variations in the boundary layer height, which influence the NO_2 vertical profile, are much lower over forested areas than, for instance, over savannas (Marion et al., 2001). Moreover, the boundary layer height usually increases throughout the day, which would lead to an overestimation of FERs, and thus, higher values in the early afternoon. The diurnal changes in AOD are negligibly small (see Fig. 12), and consequently, the effect

ACPD
13, 28453–28510, 2013

of an increasing or decreasing AOD can be ruled out. However, one possible impact of aerosols could result from changes in SSA throughout the day. The observations of FRP are higher in the early afternoon (see Fig. 3), which also increases the flaming phase consumption resulting in higher NO_x emissions compared to the morning hours. A more complete combustion further modifies the SSA (Eck et al., 2003) and potentially decreases the measurement sensitivity in polluted atmospheres, resulting in a decreased AMF (Leitão et al., 2010). Therefore, a possible explanation of the lower FERs observed for the early afternoon could be the overestimation of AMFs. However, a decrease in NO_x lifetime between morning and early afternoon could also contribute to an underestimation of early afternoon FERs for the evergreen broadleaf forest.

For the other land cover types, we mainly observe an increase in FERs between the morning and early afternoon. Obvious discrepancies in the diurnal cycle are especially found for woody savannas and savannas located in ANE, ASE, and SEA. As the boundary layer height over woody savannas tends to be larger in the afternoon, the AMFs could be underestimated, and thus, the early afternoon FERs of NO_x could be too high. Consequently, the differences between estimated morning and early afternoon FERs could at least in part be related to the underestimation of AMFs in our OMI retrieval.

Concerning the differences in morning and early afternoon FERs observed for croplands, the most plausible reason for the lower morning value in ANE is a change in the boundary layer height, as was discussed before for savannas and woody savannas. However, the higher morning value in SEA might be related to the urban/industrial released aerosols in the morning rush hours. Usually, urban/industrial aerosols have a larger SSA (Giles et al., 2012), and thus, lead to an increased measurement sensitivity.

Whether the negligible small differences in FERs for open shrublands in NAU are related to stable conditions or caused by counteracting effects is not clear.

ACPD
13, 28453–28510, 2013

In our study, we also found some differences among the selected regions for certain vegetation types. For instance, the lower values of FERs observed over NAU could be a consequence of the relatively low boundary layer heights (Labonne et al., 2007).

The influence of desert dust aerosols in ANE (see Fig. 12), which affect the retrieval of TVC NO_2, could explain the discrepancies in FERs for savanna fires between ANE and ASE. A very recent study by Bousserez (2013) shows that the Harmattan, which are prevailing surface winds bringing dry dusty air from the Sahara desert to the south, can decrease the AMF over savanna fires by 10–30 %. Bousserez (2013) explains the negative aerosol effect by the uplifted biomass burning aerosols that shielding the NO_2 concentrations below, and thus, decreasing the measurement sensitivity. According to these findings, the AMFs calculated for this study would be too high over fires in ANE (compared to ASE), and consequently, TVC NO_2 could be underestimated. The observed FERs for woody savannas are 5–10 % lower in ANE, which could be an indication of the use of too high AMFs. However, the FERs for savannas are higher in ANE than in ASE. One possible explanation for the higher values of FERs observed for savannas in ANE lies in the unexpected decreased slope beyond 300 MW pixel^{-1}, which is a unique feature among all derived FERs (see Fig. 11) and is also observed for the early afternoon (not shown). A decreased SSA resulting from an increase in both fire intensity and flaming phase consumption under highly polluted cases might be the most meaningful explanation (Leitão et al., 2010). The decrease in SSA could be lower in ANE because of the larger influence of desert dust. Therefore, the measurement sensitivity increases to a larger degree and could lead to the underestimation of TVC NO_2 and P_f. By assuming the slope between 0 and 300 MW pixel^{-1} only, the FERs would be higher for savannas, even higher than observed for ANE, and thus, confirming the findings of Bousserez (2013).

Interestingly, there are large regional discrepancies of up to 40 % observed for evergreen broadleaf forest. By assuming that the regional variations in the boundary layer height and the aerosol properties are negligibly small, and the plant characteristics are identical, it turns out, that the only reasonable explanation for these differences in FERs

ACPD
13, 28453–28510, 2013

would be a region-specific NO_x lifetime. The lower lifetime of NO_x over CSA could be the result of relatively high isoprene emissions over the Amazon rainforest (Barkley et al., 2011).

4 Summary and conclusions

In this study, a simple statistical approach has been developed to estimate NO_x emission rates and emission factors from fires using the strong correlation between the two independent geophysical parameters tropospheric NO_2 vertical column (TVC NO_2) and fire radiative power (FRP). For this, monthly average data retrieved from the measurements of four instruments (GOME-2 and OMI for TVC NO_2, MODIS Aqua and Terra for FRP) on board four different satellites, have been investigated. In general, the seasonal cycles of TVC NO_2 and FRP are strongly correlated over the biomass burning regions. In African regions, we found high correlation coefficients ($r > 0.8$) for both the morning and early afternoon state of the troposphere. Using this correlation yielded an accurate prediction of tropospheric NO_2 columns over biomass burning regions by using a simple linear regression model and FRP values. After the conversion of the TVC NO_2 into mass concentrations of NO_x, by assuming constant values for the NO_2/NO_x ratio (0.75) and lifetime of $NO_x(\tau = 6\,\mathrm{h})$, good agreement was found between the satellite derived fire emissions and GFEDv3.1 NO_x emission fields. The use of a global land cover map enabled the estimation of fire emission rates (FERs) of NO_x for different types of vegetation on a $1^\circ \times 1^\circ$ grid. The FERs have been derived for the morning and early afternoon by making use of the linear relationship between the production rate of NO_x from fire, estimated from the GOME-2 and OMI measurements, and FRP, observed by MODIS Terra and Aqua, respectively. The horizontal resolution of $1^\circ \times 1^\circ$ has been selected in order to overcome the effects of horizontal transport of NO_2 in the troposphere, and also to improve the signal to noise ratio.

Our results show that there are biome-specific, diurnal, and regional discrepancies in FERs. The estimated FERs of NO_x for the dominating types of vegeta-

ACPD
13, 28453–28510, 2013

tion burned are lowest for open shrublands (0.33–0.34 g NO_x s^{-1} MW^{-1}) and savannas (0.28–1.03 g NO_x s^{-1} MW^{-1}) and highest for croplands (0.87–1.56 g NO_x s^{-1} MW^{-1}) and woody savannas (0.82–1.54 g NO_x s^{-1} MW^{-1}). The FERs of NO_x are generally larger in the African regions than elsewhere, except for croplands where the highest values are found in SEA.

We note that the numerical values of FERs could be affected by uncertainties in both P_f and FRP, and thus, the absolute values might have considerable uncertainties. By assuming that the uncertainties in FRP observations are systematic and consistent throughout the tropical and subtropical regions selected for this study, we suggest that the diurnal discrepancies in FERs could be affected by changes in the NO_2 vertical profile and plume chemistry, whereas the regional discrepancies in estimated FERs of NO_x could at least in part be explained by differences in aerosol properties and plume chemistry.

Future efforts directed toward improving NO_2 AMFs for the satellite-based retrieval of TVC NO_2 and a better knowledge of the NO_x lifetime over biomass burning regions will improve the accuracy of FERs considerable.

In conclusion, the FERs of NO_x derived for different types of vegetation form the foundation of future efforts aimed at a new top-down based method for estimating global NO_x emissions from vegetation fires. As discussed above, the FERs are a valuable supplement to the universal emission factors, which currently do not account for spatio-temporal variations of moisture content and weather conditions. In our approach, these variations are included and averaged over the entire season. The results of this study show that the temporal relationship found between TVC NO_2 and FRP can be used for the partitioning between NO_x emissions from fire and NO_x released from other sources.

Future work will include an improved TVC NO_2 product for biomass burning, more accurate lifetimes for NO_2 based on model results, the extension to other regions (e.g. boreal regions), and an attempt to produce a global estimation of NO_x emissions from vegetation fires, based on the approach developed in this study. In general, this esti-

ACPD
13, 28453–28510, 2013

mation only requires the FRP integrated over time by including the diurnal cycle of fires and the FERs of NO_x.

Acknowledgements. Stefan F. Schreier gratefully acknowledges financial support provided by the Earth System Science Research School (ESSReS), an initiative of the Helmholtz Association of German Research Centres (HGF) at the Alfred Wegener Institute for Polar and Marine Research (AWI). Part of the work was performed within the MACC-II project, funded by the European Commission under the EU Seventh Research Framework Programme. GOME-2 lv1 data have been provided by EUMETSAT and OMI lv2 data were obtained from NASA. We also thank NASA for providing MODIS fire radiative power data. We acknowledge the use of the MODIS global land cover map and thank Xiaopeng Song for providing this product at the $1^\circ \times 1^\circ$ resolution. GRUMPv1 have been retrieved from http://sedac.ciesin.columbia.edu/gpw/global.jsp. Part of this manuscript was written while Stefan F. Schreier was hosted and financially supported by the International Institute of Advanced Systems Analysis (IIASA) in Laxenburg, Austria.

References

Akagi, S. K., Yokelson, R. J., Wiedinmyer, C., Alvarado, M. J., Reid, J. S., Karl, T., Crounse, J. D., and Wennberg, P. O.: Emission factors for open and domestic biomass burning for use in atmospheric models, Atmos. Chem. Phys., 11, 4039–4072, doi:10.5194/acp-11-4039-2011, 2011.

Alvarado, M. J. and Prinn, R. G.: Formation of ozone and growth of aerosols in young smoke plumes from biomass burning: 1. Lagrangian parcel studies, J. Geophys. Res.-Atmos., 114, D09306, doi:10.1029/2008JD011144, 2009.

Andreae, M. O. and Merlet, P.: Emission of trace gases and aerosols from biomass burning, Global Biogeochem. Cy., 15, 955–966, 2001.

Barkley, M. P., Palmer, P. I., Ganzeveld, L., Arneth, A., Hagberg, D., Karl, T., Guenther, A., Paulot, F., Wennberg, P. O., Mao, J., Kurosu, T. P., Chance, K., Müller, J. F., De Smedt, I., Van Roozendael, M., Chen, D., Wang, Y., and Yantosca, R. M.: Can a "state of the art" chemistry transport model simulate Amazonian tropospheric chemistry?, J. Geophys. Res.-Atmos., 116, D16302, doi:10.1029/2011JD015893, 2011.

ACPD
13, 28453–28510, 2013

Beirle, S., Platt, U., Wenig, M., and Wagner, T.: NO_x production by lightning estimated with GOME, Adv. Space Res., 34, 793–797, 2004.
Beirle, S., Boersma, K. F., Platt, U., Lawrence, M. G., and Wagner, T.: Megacity emissions and lifetimes of nitrogen oxides probed from space, Science, 333, 1737–1739, 2011.
Boersma, K. F., Eskes, H. J., and Brinksma, E. J.: Error analysis for tropospheric NO_2 retrieval from space, J. Geophys. Res.-Atmos., 109, D04311, 4311–4320, 2004.
Boersma, K. F., Jacob, D. J., Eskes, H. J., Pinder, R. W., Wang, J., and van der A, R. J.: Intercomparison of SCIAMACHY and OMI tropospheric NO_2 columns: observing the diurnal evolution of chemistry and emissions from space, J. Geophys. Res.-Atmos., 113, D16S26, doi:10.1029/2007JD008816, 2008.
Bousserez, N.: Space-based retrieval of NO_2 over biomass burning regions: quantifying and reducing uncertainties, Atmos. Meas. Tech. Discuss., 6, 6645–6684, doi:10.5194/amtd-6-6645-2013, 2013.
Bovensmann, H., Burrows, J. P., Buchwitz, M., Frerick, J., Noël, S., Rozanov, V. V., Chance, K. V., and Goede, A. P. H.: SCIAMACHY: mission objectives and measurement modes, J. Atmos. Sci., 56, 127–150, 1999.
Browne, E. C. and Cohen, R. C.: Effects of biogenic nitrate chemistry on the NO_x lifetime in remote continental regions, Atmos. Chem. Phys., 12, 11917–11932, doi:10.5194/acp-12-11917-2012, 2012.
Bucsela, E. J., Celarier, E. A., Wenig, M. O., Gleason, J. F., Veefkind, J. P., Boersma, K. F., and Brinksma, E. J.: Algorithm for NO_2 vertical column retrieval from the ozone monitoring instrument, IEEE T. Geosci. Remote, 44, 1245–1257, 2006.
Burrows, J. P., Hölzle, E., Goede, A. P. H., Visser, H., and Fricke, W.: SCIAMACHY-scanning imaging absorption spectrometer for atmospheric chartography, Acta Astron., 35, 445–451, 1995.
Burrows, J. P., Weber, M., Buchwitz, M., Rozanov, V., Ladstätter-Weißenmayer, A., Richter, A., Debeek, R., Hoogen, R., Bramstedt, K., Eichmann, K. U., Eisinger, M., and Perner, D.: The Global Ozone Monitoring Experiment (GOME): mission concept and first scientific results, J. Atmos. Sci., 56, 151–175, 1999.
Cahoon Jr, D. R., Stocks, B. J., Levine, J. S., Cofer III, W. R., and O'Neill, K. P.: Seasonal distribution of African savanna fires, Nature, 359, 812–815, 1992.
Callies, J., Corpaccioli, E., Eisinger, M., Lefebvre, A., Munro, R., Perez-Albinana, A., Ricciarelli, B., Calamai, L., Gironi, G., Veratti, R., Otter, G., Eschen, M., and Van Riel, L.: GOME-2

ACPD
13, 28453–28510, 2013

ozone instrument on-board the European METOP satellites, in: Weather and Environemental Satellites, Proceedings of SPIE – The International Society for Optical Engineering, Denver, CO, 60–70, 2004.
Cançado, J. E. D., Saldiva, P. H. N., Pereira, L. A. A., Lara, L. B. L. S., Artaxo, P., Martinelli, L. A., Arbex, M. A., Zanobetti, A., and Braga, A. L. F.: The impact of sugar cane-burning emissions on the respiratory system of children and the elderly, Environ. Health Persp., 114, 725–729, 2006.
Crutzen, P. J. and Andreae, M. O.: Biomass burning in the tropics: impact on atmospheric chemistry and biogeochemical cycles, Science, 250, 1669–1678, 1990.
Eck, T. F., Holben, B. N., Reid, J. S., O'Neill, N. T., Schafer, J. S., Dubovik, O., Smirnov, A., Yamasoe, M. A., and Artaxo, P.: High aerosol optical depth biomass burning events: a comparison of optical properties for different source regions, Geophys. Res. Lett., 30, 2035, doi:10.1029/2003GL017861, 2003.
Freeborn, P. H., Wooster, M. J., and Roberts, G.: Addressing the spatiotemporal sampling design of MODIS to provide estimates of the fire radiative energy emitted from Africa, Remote Sens. Environ., 115, 475–489, 2011.
Friedl, M. A., Sulla-Menashe, D., Tan, B., Schneider, A., Ramankutty, N., Sibley, A., and Huang, X.: MODIS collection 5 global land cover: algorithm refinements and characterization of new datasets, Remote Sens. Environ., 114, 168–182, 2010.
Giglio, L.: Characterization of the tropical diurnal fire cycle using VIRS and MODIS observations, Remote Sens. Environ., 108, 407–421, 2007.
Giglio, L., van der Werf, G. R., Randerson, J. T., Collatz, G. J., and Kasibhatla, P.: Global estimation of burned area using MODIS active fire observations, Atmos. Chem. Phys., 6, 957–974, doi:10.5194/acp-6-957-2006, 2006.
Giglio, L., Randerson, J. T., van der Werf, G. R., Kasibhatla, P. S., Collatz, G. J., Morton, D. C., and DeFries, R. S.: Assessing variability and long-term trends in burned area by merging multiple satellite fire products, Biogeosciences, 7, 1171–1186, doi:10.5194/bg-7-1171-2010, 2010.
Giles, D. M., Holben, B. N., Eck, T. F., Sinyuk, A., Smirnov, A., Slutsker, I., Dickerson, R. R., Thompson, A. M., and Schafer, J. S.: An analysis of AERONET aerosol absorption properties and classifications representative of aerosol source regions, J. Geophys. Res.-Atmos., 117, D17203, doi:10.1029/2012JD018127, 2012.

ACPD
13, 28453–28510, 2013

Guenther, A., Karl, T., Harley, P., Wiedinmyer, C., Palmer, P. I., and Geron, C.: Estimates of global terrestrial isoprene emissions using MEGAN (Model of Emissions of Gases and Aerosols from Nature), Atmos. Chem. Phys., 6, 3181–3210, doi:10.5194/acp-6-3181-2006, 2006.

Hains, J. C., Boersma, K. F., Mark, K., Dirksen, R. J., Cohen, R. C., Perring, A. E., Bucsela, E., Volten, H., Swart, D. P. J., Richter, A., Wittrock, F., Schoenhardt, A., Wagner, T., Ibrahim, O. W., Roozendael, M. V., Pinardi, G., Gleason, J. F., Veefkind, J. P., and Levelt, P.: Testing and improving OMI DOMINO tropospheric NO_2 using observations from the DANDELIONS and INTEX-B validation campaigns, J. Geophys. Res.-Atmos., 115, D05301, doi:10.1029/2009JD012399, 2010.

Hansen, M. C., Defries, R. S., Townshend, J. R. G., and Sohlberg, R.: Global land cover classification at 1 km spatial resolution using a classification tree approach, Int. J. Remote Sens., 21, 1331–1364, 2000.

Heue, K.-P., Richter, A., Bruns, M., Burrows, J. P., v. Friedeburg, C., Platt, U., Pundt, I., Wang, P., and Wagner, T.: Validation of SCIAMACHY tropospheric NO_2-columns with AMAXDOAS measurements, Atmos. Chem. Phys., 5, 1039–1051, doi:10.5194/acp-5-1039-2005, 2005.

Heue, K.-P., Wagner, T., Broccardo, S. P., Walter, D., Piketh, S. J., Ross, K. E., Beirle, S., and Platt, U.: Direct observation of two dimensional trace gas distributions with an airborne Imaging DOAS instrument, Atmos. Chem. Phys., 8, 6707–6717, doi:10.5194/acp-8-6707-2008, 2008.

Hilboll, A., Richter, A., Rozanov, A., Hodnebrog, Ø., Heckel, A., Solberg, S., Stordal, F., and Burrows, J. P.: Improvements to the retrieval of tropospheric NO_2 from satellite – stratospheric correction using SCIAMACHY limb/nadir matching and comparison to Oslo CTM2 simulations, Atmos. Meas. Tech., 6, 565–584, doi:10.5194/amt-6-565-2013, 2013.

Hönninger, G., von Friedeburg, C., and Platt, U.: Multi axis differential optical absorption spectroscopy (MAX-DOAS), Atmos. Chem. Phys., 4, 231–254, doi:10.5194/acp-4-231-2004, 2004.

Ichoku, C. and Kaufman, Y. J.: A method to derive smoke emission rates from MODIS fire radiative energy measurements, IEEE T. Geosci. Remote, 43, 2636–2649, 2005.

Ichoku, C., Kahn, R., and Chin, M.: Satellite contributions to the quantitative characterization of biomass burning for climate modeling, Atmos. Res., 111, 1–28, 2012.

Inness, A., Baier, F., Benedetti, A., Bouarar, I., Chabrillat, S., Clark, H., Clerbaux, C., Coheur, P., Engelen, R. J., Errera, Q., Flemming, J., George, M., Granier, C., Hadji-Lazaro, J., Huij-

ACPD
13, 28453–28510, 2013

nen, V., Hurtmans, D., Jones, L., Kaiser, J. W., Kapsomenakis, J., Lefever, K., Leitão, J., Razinger, M., Richter, A., Schultz, M. G., Simmons, A. J., Suttie, M., Stein, O., Thépaut, J.-N., Thouret, V., Vrekoussis, M., Zerefos, C., and the MACC team: The MACC reanalysis: an 8 yr data set of atmospheric composition, Atmos. Chem. Phys., 13, 4073–4109, doi:10.5194/acp-13-4073-2013, 2013.

IPCC: Climate Change 2007: The Physical Science Basis, contribution of Working Group I to the Fourth Assessment Report of the Intergovernmental Panel on Climate Change, edited by: Solomon, S., Qin, D., Manning, M., Chen, Z., Marquis, M., Averyt, K. B., Tignor, M., and Miller, H. L., Cambridge Univ. Press, Cambridge, UK and New York, USA, 2007.

Jaeglé, L., Steinberger, L., Martin, R. V., and Chance, K.: Global partitioning of NO_x sources using satellite observations: relative roles of fossil fuel combustion, biomass burning and soil emissions, Faraday Discuss., 130, 407–423, 2005.

Justice, C. O., Giglio, L., Korontzi, S., Owens, J., Morisette, J. T., Roy, D., Descloitres, J., Alleaume, S., Petitcolin, F., and Kaufman, Y.: The MODIS fire products, Remote Sens. Environ., 83, 244–262, 2002.

Kaiser, J. W., Heil, A., Andreae, M. O., Benedetti, A., Chubarova, N., Jones, L., Morcrette, J.-J., Razinger, M., Schultz, M. G., Suttie, M., and van der Werf, G. R.: Biomass burning emissions estimated with a global fire assimilation system based on observed fire radiative power, Biogeosciences, 9, 527–554, doi:10.5194/bg-9-527-2012, 2012.

Kaufman, Y. J., Justice, C. O., Flynn, L. P., Kendall, J. D., Prins, E. M., Giglio, L., Ward, D. E., Menzel, W. P., and Setzer, A. W.: Potential global fire monitoring from EOS-MODIS, J. Geophys. Res.-Atmos., 103, 32215–32238, 1998.

Koelemeijer, R. B. A., de Haan, J. F., and Stammes, P.: A database of spectral surface reflectivity in the range 335–772 nm derived from 5.5 yr of GOME observations, J. Geophys. Res.-Atmos., 108, 4070, doi:10.1029/2002JD002429, 2003.

Korontzi, S., Ward, D. E., Susott, R. A., Yokelson, R. J., Justice, C. O., Hobbs, P. V., Smithwick, E. A. H., and Hao, W. M.: Seasonal variation and ecosystem dependence of emission factors for selected trace gases and $PM_{2.5}$ for southern African savanna fires, J. Geophys. Res.-Atmos., 108, 4758, doi:10.1029/2003JD003730, 2003.

Künzli, N., Kaiser, R., Medina, S., Studnicka, M., Chanel, O., Filliger, P., Herry, M., Horak Jr, F., Puybonnieux-Texier, V., Quénel, P., Schneider, J., Seethaler, R., Vergnaud, J. C., and Sommer, H.: Public-health impact of outdoor and traffic-related air pollution: a European assessment, Lancet, 356, 795–801, 2000.

ACPD
13, 28453–28510, 2013

Labonne, M., Bréon, F. M., and Chevallier, F.: Injection height of biomass burning aerosols as seen from a spaceborne lidar, Geophys. Res. Lett., 34, L11806, doi:10.1029/2007GL029311, 2007.
Langmann, B., Duncan, B., Textor, C., Trentmann, J., and van der Werf, G. R.: Vegetation fire emissions and their impact on air pollution and climate, Atmos. Environ., 43, 107–116, 2009.
Lee, D. S., Köhler, I., Grobler, E., Rohrer, F., Sausen, R., Gallardo-Klenner, L., Olivier, J. G. J., Dentener, F. J., and Bouwman, A. F.: Estimations of global NO_x emissions and their uncertainties, Atmos. Environ., 31, 1735–1749, 1997.
Leighton, P. A.: Photochemistry of Air Pollution, Academic, New York, 1961.
Leitão, J., Richter, A., Vrekoussis, M., Kokhanovsky, A., Zhang, Q. J., Beekmann, M., and Burrows, J. P.: On the improvement of NO_2 satellite retrievals – aerosol impact on the airmass factors, Atmos. Meas. Tech., 3, 475–493, doi:10.5194/amt-3-475-2010, 2010.
Levelt, P. F., Van Den Oord, G. H. J., Dobber, M. R., Mälkki, A., Visser, H., De Vries, J., Stammes, P., Lundell, J. O. V., and Saari, H.: The ozone monitoring instrument, IEEE T. Geosci. Remote, 44, 1093–1100, 2006.
Marais, E. A., Jacob, D. J., Kurosu, T. P., Chance, K., Murphy, J. G., Reeves, C., Mills, G., Casadio, S., Millet, D. B., Barkley, M. P., Paulot, F., and Mao, J.: Isoprene emissions in Africa inferred from OMI observations of formaldehyde columns, Atmos. Chem. Phys., 12, 6219–6235, doi:10.5194/acp-12-6219-2012, 2012.
Marion, T., Perros, P. E., Losno, R., and Steiner, E.: Ozone production efficiency in savanna and forested areas during the EXPRESSO experiment, J. Atmos. Chem., 38, 3–30, 2001.
Martin, R. V., Jacob, D. J., Chance, K., Kurosu, T. P., Palmer, P. I., and Evans, M. J.: Global inventory of nitrogen oxide emissions constrained by space-based observations of NO_2 columns, J. Geophys. Res.-Atmos., 108, 4537, doi:10.1029/2003JD003453, 2003.
Mebust, A. K. and Cohen, R. C.: Observations of a seasonal cycle in NO_x emissions from fires in African woody savannas, Geophys. Res. Lett., 40, 1451–1455, 2013a.
Mebust, A. K. and Cohen, R. C.: Space-based observations of fire NO_x emission coefficients: a global biome-scale comparison, Atmos. Chem. Phys. Discuss., 13, 21665–21702, doi:10.5194/acpd-13-21665-2013, 2013b.
Mebust, A. K., Russell, A. R., Hudman, R. C., Valin, L. C., and Cohen, R. C.: Characterization of wildfire NO_x emissions using MODIS fire radiative power and OMI tropospheric NO_2 columns, Atmos. Chem. Phys., 11, 5839–5851, doi:10.5194/acp-11-5839-2011, 2011.

ACPD
13, 28453–28510, 2013

Meland, B. R. and Boubel, R. W.: A study of field burning under varying environmental conditions, J. Air Pollut. Contr. Assoc., 16, 9, 481–484, 1966.
Meyer-Arnek, J., Ladstätter-Weißenmayer, A., Richter, A., Wittrock, F., and Burrows, J. P.: A study of the trace gas columns of O_3, NO_2 and HCHO over Africa in September 1997, Faraday Discuss., 130, 387–405, 2005.
Munro, R., Perez Albiñana, A., Callies, J., Corpaccioli, E., Eisinger, M., Lefebvre, A., and Hahne, A.: Expectations for GOME-2 on the METOP Satellites, in: ERS-Envisat Symposium "Looking Down to Earth in the New Millennium", European Space Agency, (Special Publication) ESA SP, Gothenburg, 221–227, 2000.
Nüß, J. H.: Improvements of the retrieval of tropospheric NO_2 from GOME and SCIAMACHY data, Ph.D. Thesis, University of Bremen, Bremen, Germany, 2005.
Olivier, J. G. J., Bouwman, A. F., Van der Maas, C. W. M., and Berdowski, J. M.: Emission database for global Atmospheric Research (EDGAR), Environ. Monit. Assess., 31, 93–106, 1994.
Perner, D. and Platt, U.: Detection of nitrous acid in the atmosphere by differential optical absorption, Geophys. Res. Lett., 6, 917–920, 1979.
Platt, U. and Hausmann, M.: Spectroscopic measurement of the free radicals NO_3, BrO, IO, and OH in the troposphere, Res. Chem. Intermed., 20, 557–578, 1994.
Remer, L. A., Kleidman, R. G., Levy, R. C., Kaufman, Y. J., Tanré, D., Mattoo, S., Martins, J. V., Ichoku, C., Koren, I., Yu, H., and Holben, B. N.: Global aerosol climatology from the MODIS satellite sensors, J. Geophys. Res.-Atmos., 113, D14S07, doi:10.1029/2007JD009661, 2008.
Richter, A. and Burrows, J. P.: Tropospheric NO_2 from GOME measurements, Adv. Space Res., 29, 1673–1683, 2002.
Richter, A., Begoin, M., Hilboll, A., and Burrows, J. P.: An improved NO_2 retrieval for the GOME-2 satellite instrument, Atmos. Meas. Tech., 4, 1147–1159, doi:10.5194/amt-4-1147-2011, 2011.
Riggan, P. J., Tissell, R. G., Lockwood, R. N., Brass, J. A., Pereira, J. A. R., Miranda, H. S., Miranda, A. C., Campos, T., and Higgins, R.: Remote measurement of energy and carbon flux from wildfires in Brazil, Ecol. Appl., 14, 855–872, 2004.
Roberts, G. J. and Wooster, M. J.: Fire detection and fire characterization over Africa using meteosat SEVIRI, IEEE T. Geosci. Remote, 46, 1200–1218, 2008.

ACPD
13, 28453–28510, 2013

Roberts, G., Wooster, M. J., and Lagoudakis, E.: Annual and diurnal african biomass burning temporal dynamics, Biogeosciences, 6, 849–866, doi:10.5194/bg-6-849-2009, 2009.
Row, L. W., Hastings, D. A., and Dunbar, P. K.: Terrainbase worldwide digital terrain data, Release 1.0., National Geophysical Data Center, Boulder, 1994.
Sahu, L. K., Kondo, Y., Miyazaki, Y., Pongkiatkul, P., and Kim Oanh, N. T.: Seasonal and diurnal variations of black carbon and organic carbon aerosols in Bangkok, J. Geophys. Res.-Atmos., 116, D15302, doi:10.1029/2010JD015563, 2011.
Schroeder, W., Csiszar, I., Giglio, L., and Schmidt, C. C.: On the use of fire radiative power, area, and temperature estimates to characterize biomass burning via moderate to coarse spatial resolution remote sensing data in the Brazilian Amazon, J. Geophys. Res.-Atmos., 115, D21121, doi:10.1029/2009JD013769, 2010.
Seiler, W. and Crutzen, P. J.: Estimates of gross and net fluxes of carbon between the biosphere and the atmosphere from biomass burning, Climatic Change, 2, 207–247, 1980.
Spicer, C. W.: Nitrogen oxide reactions in the urban plume of Boston, Science, 215, 1095–1097, 1982.
van der A, R. J., Eskes, H. J., Boersma, K. F., van Noije, T. P. C., Van Roozendael, M., De Smedt, I., Peters, D. H. M. U., and Meijer, E. W.: Trends, seasonal variability and dominant NO_x source derived from a ten year record of NO_2 measured from space, J. Geophys. Res.-Atmos., 113, D04302, doi:10.1029/2007JD009021, 2008.
van der Werf, G. R., Randerson, J. T., Giglio, L., Collatz, G. J., Mu, M., Kasibhatla, P. S., Morton, D. C., DeFries, R. S., Jin, Y., and van Leeuwen, T. T.: Global fire emissions and the contribution of deforestation, savanna, forest, agricultural, and peat fires (1997–2009), Atmos. Chem. Phys., 10, 11707–11735, doi:10.5194/acp-10-11707-2010, 2010.
Wang, P., Richter, A., Bruns, M., Rozanov, V. V., Burrows, J. P., Heue, K.-P., Wagner, T., Pundt, I., and Platt, U.: Measurements of tropospheric NO_2 with an airborne multi-axis DOAS instrument, Atmos. Chem. Phys., 5, 337–343, doi:10.5194/acp-5-337-2005, 2005.
Wang, P., Stammes, P., van der A, R., Pinardi, G., and van Roozendael, M.: FRESCO+: an improved O_2 A-band cloud retrieval algorithm for tropospheric trace gas retrievals, Atmos. Chem. Phys., 8, 6565–6576, doi:10.5194/acp-8-6565-2008, 2008.
Wayne, R. P., Barnes, I., Biggs, P., Burrows, J. P., Canosa-Mas, C. E., Hjorth, J., Le Bras, G., Moortgat, G. K., Perner, D., Poulet, G., Restelli, G., and Sidebottom, H.: The nitrate radical: physics, chemistry, and the atmosphere, Atmos. Environ., 25, 1-203, 1991.

ACPD
13, 28453–28510, 2013

Wittrock, F., Oetjen, H., Richter, A., Fietkau, S., Medeke, T., Rozanov, A., and Burrows, J. P.: MAX-DOAS measurements of atmospheric trace gases in Ny-Ålesund - Radiative transfer studies and their application, Atmos. Chem. Phys., 4, 955–966, doi:10.5194/acp-4-955-2004, 2004.

Wooster, M. J. and Zhang, Y. H.: Boreal forest fires burn less intensely in Russia than in North America, Geophys. Res. Lett., 31, L20505, 20501–20503, 2004.

Wooster, M. J., Roberts, G., Perry, G. L. W., and Kaufman, Y. J.: Retrieval of biomass combustion rates and totals from fire radiative power observations: FRP derivation and calibration relationships between biomass consumption and fire radiative energy release, J. Geophys. Res.-Atmos., 110, 1–24, 2005.

Xu, W., Wooster, M. J., Roberts, G., and Freeborn, P.: New GOES imager algorithms for cloud and active fire detection and fire radiative power assessment across North, South and Central America, Remote Sens. Environ., 114, 1876–1895, 2010.

Yienger, J. J. and Levy II, H.: Empirical model of global soil-biogenic NO_x emissions, J. Geophys. Res., 100, 11447–11464, 1995.

ACPD
13, 28453–28510, 2013

Table 1. Selected regions with their abbreviation, location, and absolute area.

Region	Abbreviation	Latitudes	Longitudes	Area [km^2]
Africa north of equator	ANE	0° to 10° N	15° W to 40° E	6.76×10^6
Africa south of equator	ASE	20° S to 5° S	10° E to 40° E	5.41×10^6
central South America	CSA	15° S to 0°	65° W to 35° W	5.49×10^6
northern Australia	NAU	25° S to 15° S	120° E to 145° E	2.90×10^6
Southeast Asia	SEA	10° N to 25° N	90° E to 110° E	3.53×10^6

ACPD
13, 28453–28510, 2013

Table 2. Absolute numbers of 1° × 1° boxes included in the analysis for the estimation of fire emission rates (FERs) of NO_x for the different types of vegetation and the selected regions extracted from the Collection 5 MODIS Land Cover Type product. FERs of NO_x obtained from the morning (early afternoon) observations are shown left (right).

Land cover type	ANE	ASE	CSA	NAU	SEA
evergreen broadleaf forest	2258/4129	286/294	9999/9509	–/–	2484/3322
open shrublands	–/60	240/300	–/–	7080/6780	–/–
woody savannas	6365/6462	12 608/12 708	60/60	240/180	1860/2154
savannas	5028/5039	8797/8758	9964/9470	1800/1679	–/–
croplands	1136/980	–/–	–/117	–/–	950/893

ACPD
13, 28453–28510, 2013

Table 3. Mean gradients (FERs), in $g\,NO_x\,s^{-1}\,MW^{-1}$, derived from the best fitting least-squares regression lines for each land cover type and the selected regions, applying the morning (left) and early afternoon (right) linear relationships between P_f and FRP.

Land cover type	ANE	ASE	CSA	NAU	SEA
evergreen broadleaf forest	0.94/0.77	–/–	0.55/0.43	–/–	0.76/0.60
open shrublands	–/–	–/–	–/–	0.33/0.34	–/–
woody savannas	0.84/1.41	0.88/1.54	–/–	–/–	0.82/1.18
savannas	0.62/1.03	0.48/0.84	0.53/0.49	0.35/0.28	–/–
croplands	0.87/1.19	–/–	–/–	–/–	1.56/1.22

ACPD
13, 28453–28510, 2013

Table 4. Emission factors (EFs) of NO_x as calculated from the morning and early afternoon satellite-derived FERs, EFs from Andreae and Merlet (2001), and EFs from Akagi et al. (2011).

Land cover type (UMD)	Morning[a,b] (this study)	Early afternoon[a,b] (this study)	Andreae and Merlet[b] (2001)	Akagi[b] (2011)	Land cover type (literature)
evergreen broadleaf forest	0.57–0.98	0.44–0.8	1.6 ± 0.7	2.55 ± 1.4	tropical forest
open shrublands	0.63	0.65			
woody savannas	1.57–1.69	2.27–2.96	3.9 ± 2.4	3.9 ± 0.8	savanna and grassland
savannas	0.67–1.19	0.53–1.98			
croplands	4.14–7.4	5.64–5.79	2.5 ± 1.0	3.11 ± 1.57	crop residue

[a] calculations are based on biome-specific conversion factors (Kaiser et al., 2012).
[b] EFs of NO_x are presented as NO.

ACPD
13, 28453–28510, 2013

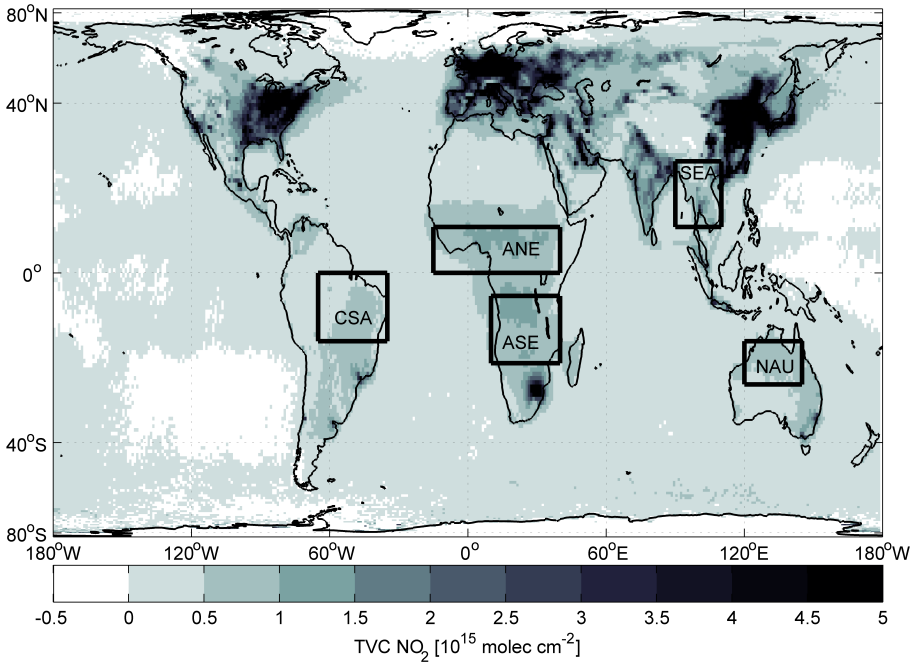

Fig. 1. Global mean tropospheric NO_2 vertical columns (2007–2011) retrieved from GOME-2 measurements. Africa north of equator (ANE, 0° to 10° N and 15° W to 40° E), Africa south of equator (ASE, 20° S to 5° S and 10° E to 40° E), central South America (CSA, 15° S to 0° and 65° W to 35° W), northern Australia (NAU, 25° S to 15° S and 120° E to 145° E), and Southeast Asia (SEA, 10° N to 25° N and 90° E to 110° E) are highlighted by black rectangles (see also Table 1).

ACPD
13, 28453–28510, 2013

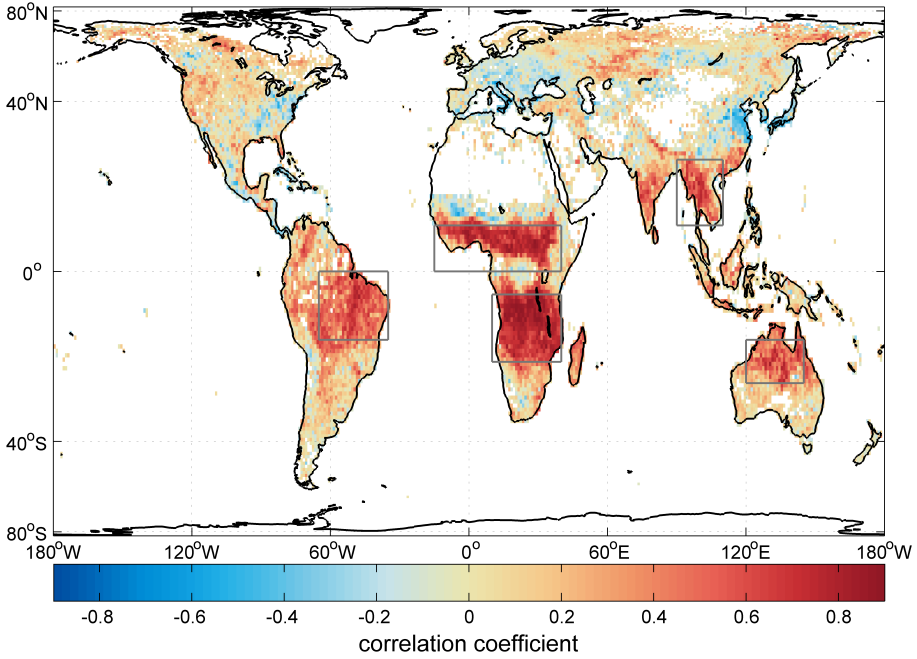

Fig. 2. Correlation coefficients (r) of the local temporal relationship between FRP and TVC NO_2 based on monthly averages from 2007–2011 on a $1^\circ \times 1^\circ$ grid. Data are shown for the linear relationship observed between GOME-2 TVC NO_2 and MODIS Terra FRP.

ACPD
13, 28453–28510, 2013

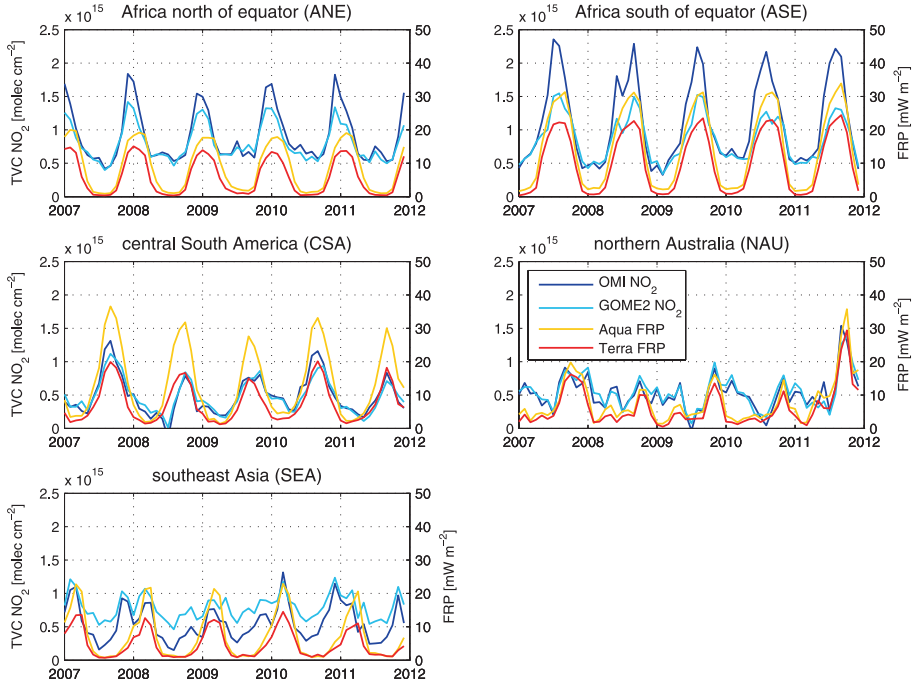

Fig. 3. Temporal variability of MODIS Terra (red) and MODIS Aqua (orange) derived FRP and GOME-2 (turquois) and OMI (blue) derived TVC NO_2 for the selected regions as highlighted in Fig. 1 and defined in Table 1.

ACPD
13, 28453–28510, 2013

Empirical estimates of fire emission rates of NO_x

S. F. Schreier et al.

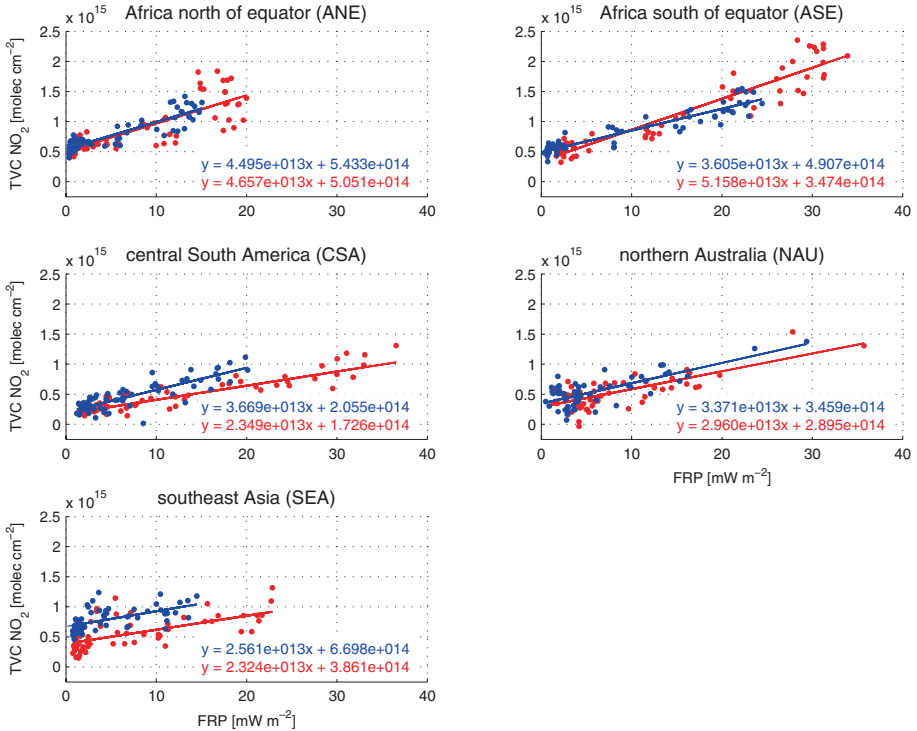

Fig. 4. Scatter plots with their associated regression coefficients for the selected regions, illustrating the linear relationship of GOME-2 TVC NO_2 vs. MODIS Terra FRP (blue) as well as OMI TVC NO_2 vs. MODIS Aqua FRP (red). Each dot represents a monthly average over the respective region.

ACPD
13, 28453–28510, 2013

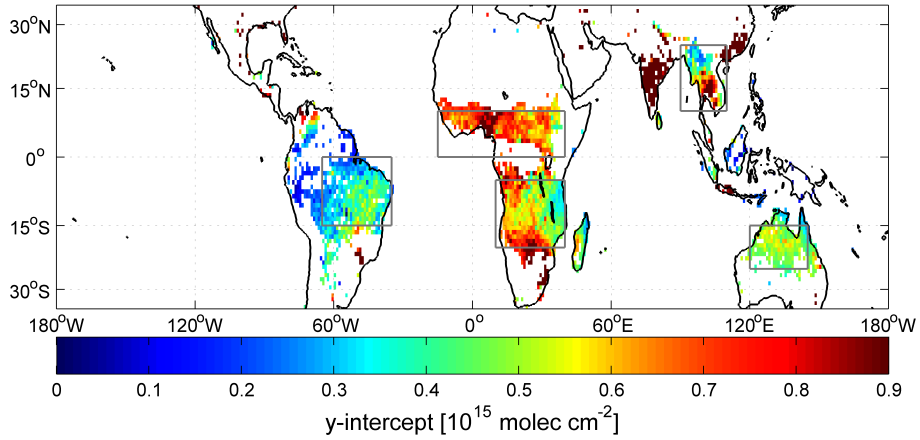

Fig. 5. Mean *y*-intercepts [in units of 10^{15} molecules cm^{-2}] of the best fitting least-squares regression lines (2007–2011) for pixels with $r > 0.3$, based on a $1^\circ \times 1^\circ$ grid. Data are shown for the regression lines between GOME-2 TVC NO_2 and MODIS Terra FRP.

ACPD
13, 28453–28510, 2013

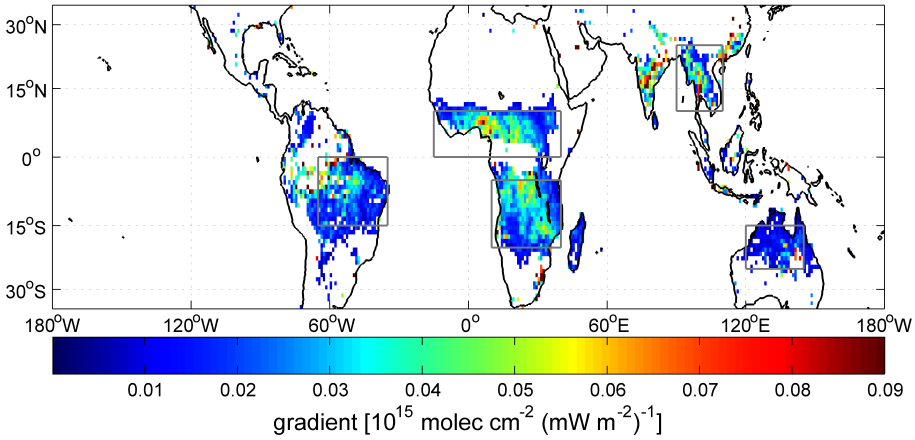

Fig. 6. Mean gradients [in units of 10^{15} molecules cm^{-2} $(mW\,m^{-2})^{-1}$] of the best fitting least-squares regression lines (2007–2011) for pixels with $r > 0.3$, based on a $1^\circ \times 1^\circ$ grid. Data are shown for GOME-2 TVC NO_2 vs. MODIS Terra FRP linear relationships.

ACPD
13, 28453–28510, 2013

Empirical estimates of fire emission rates of NO_x

S. F. Schreier et al.

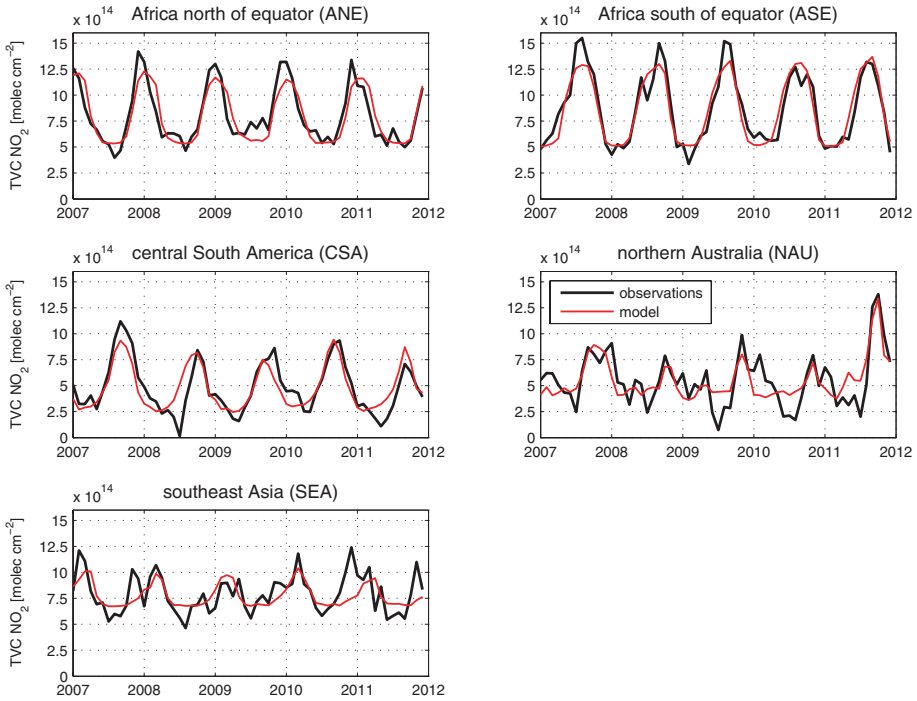

Fig. 7. Monthly means of TVC NO_2 from GOME-2 measurements (black line) and TVC NO_2 as calculated from the simple linear model (red line) for the selected regions.

ACPD
13, 28453–28510, 2013

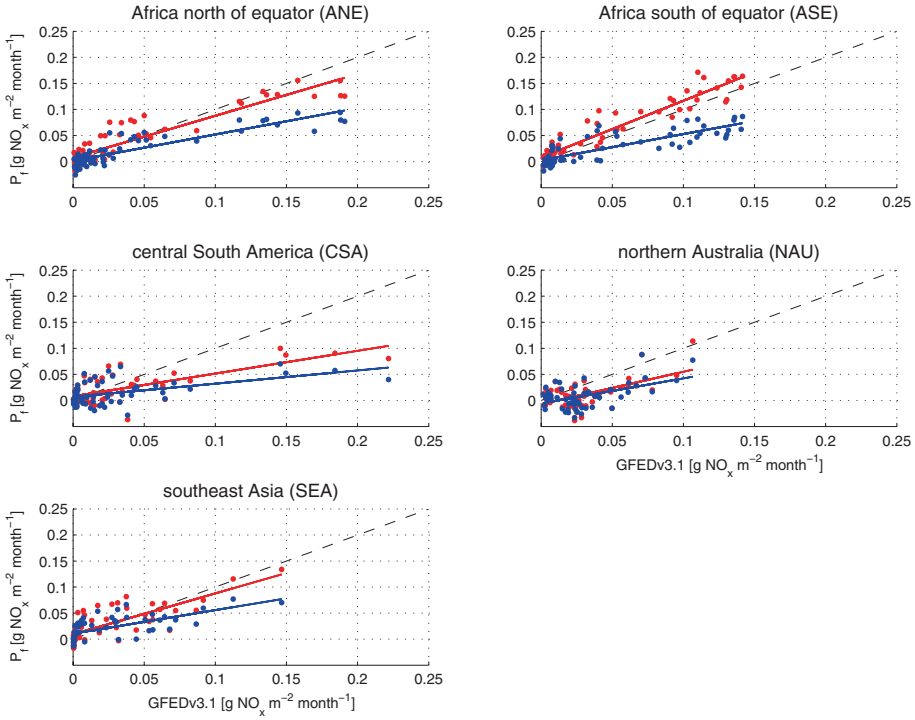

Fig. 8. Scatter plots of the estimated monthly production rates of NO_x from fires (P_f), retrieved from the GOME-2 (blue) and OMI (red) TVC NO_2 observations, against GFED3.1 NO_x emission fields. The 1 : 1 line is shown by the dashed black line.

ACPD
13, 28453–28510, 2013

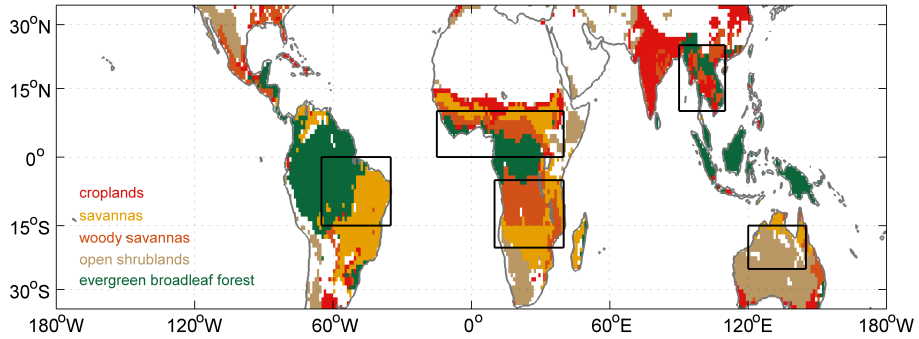

Fig. 9. Global land cover map used for the distinction of the different biomes (see also Sect. 2.3 and Table 2). The selected land cover types are evergreen broadleaf forest (green), open shrublands (beige), woody savannas (orange), savannas (yellow), and croplands (red).

ACPD
13, 28453–28510, 2013

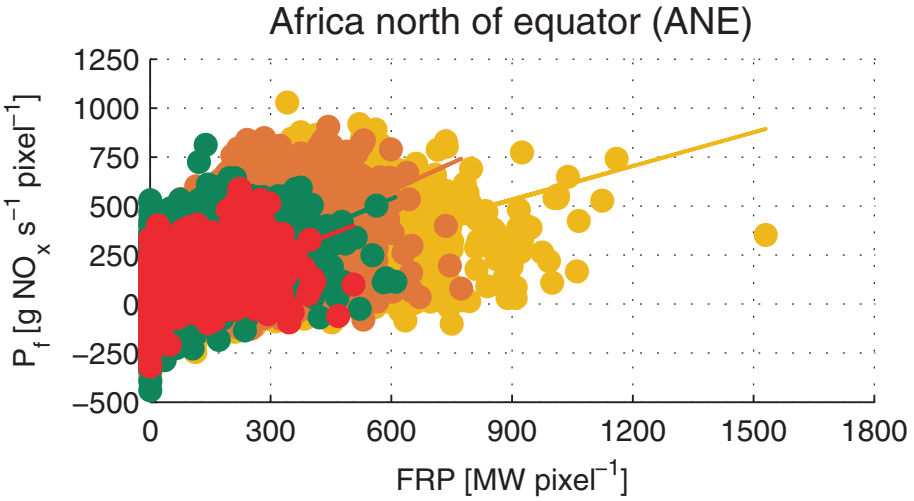

Fig. 10. Biome-specific FERs of NO_x for ANE. Here, the best fitting least-squares regression lines of the morning observations (GOME-2 vs. MODIS Terra) are shown for evergreen broadleaf forest (green), woody savannas (orange), savannas (yellow), and croplands (red).

ACPD
13, 28453–28510, 2013

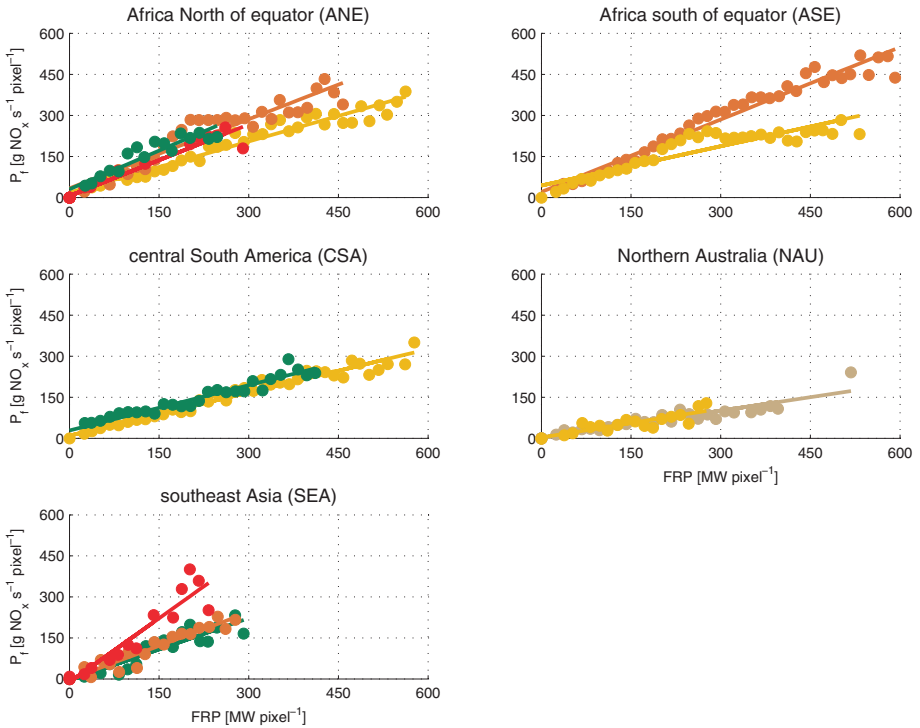

Fig. 11. Biome-specific FERs of NO_x, averaged via the binning method, for the selected regions. Here, the best fitting least-squares regression lines of the morning observations (GOME-2 vs. MODIS Terra) are shown for evergreen broadleaf forest (green), open shrublands (beige), woody savannas (orange), savannas (yellow), and croplands (red). The binning method used for the averaging is described in the text.

ACPD
13, 28453–28510, 2013

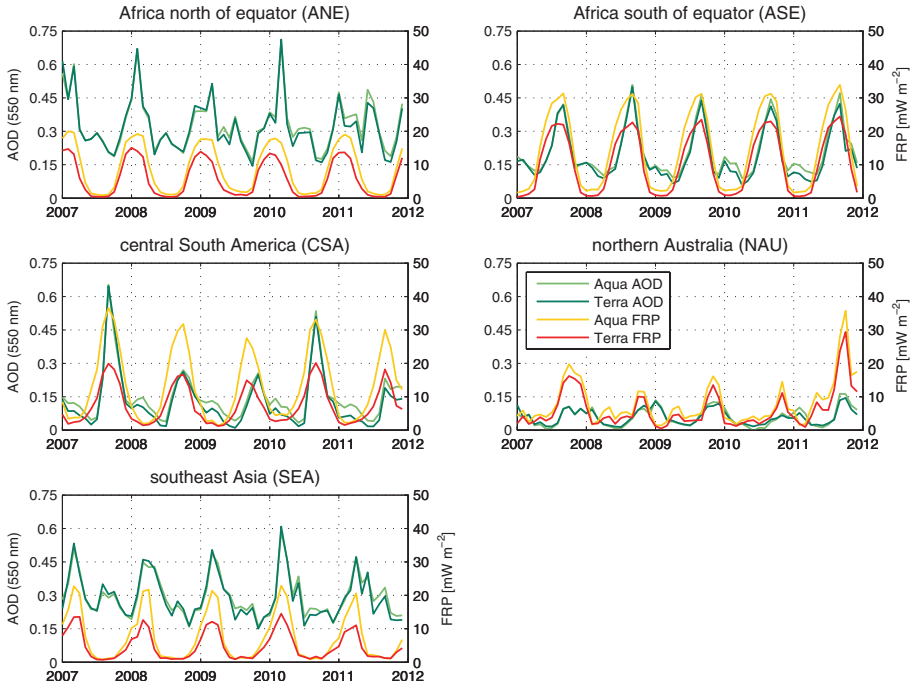

Fig. 12. Temporal variability of MODIS Terra (red) and MODIS Aqua (orange) derived FRP and MODIS Terra (dark green) and MODIS Aqua (light green) derived AOD for ANE, ASE, CSA, NAU, and SEA.

ACPD
13, 28453–28510, 2013